High-Resolution Meteorological Monitoring over the National Capital Region: Data from the DCNet Network at the US Department of Commerce Herbert C. Hoover Building Station

Will Pendergrass[1]
Nebila Lichiheb[1]
Randy White[1]
Bruce B. Hicks[2]
LaToya Myles[1]

August 2020

National Oceanic and Atmospheric Administration
Office of Oceanic and Atmospheric Research
Air Resources Laboratory
Atmospheric Turbulence and Diffusion Division
Oak Ridge, Tennessee

1 NOAA/ARL/ATDD 456 S. Illinois Ave, Oak Ridge, TN
2 MetCorps, P.O. Box 1510 Norris, TN

High-Resolution Meteorological Monitoring over the National Capital Region: Data from the DCNet Network at the US Department of Commerce Herbert C. Hoover Building Station

By Will Pendergrass, Nebila Lichiheb, Randy White, Bruce B. Hicks, and LaToya Myles

August 2020

National Oceanic and Atmospheric Administration
Oceanic and Atmospheric Research
Air Resources Laboratory
Atmospheric Turbulence and Diffusion Division
Oak Ridge, Tennessee

U.S. Department of Commerce
Secretary of Commerce Wilbur Ross

Under Secretary for Oceans and Atmosphere/Acting NOAA Administrator
Dr. Neil Jacobs

Assistant Secretary for Oceans and Atmosphere/Deputy NOAA Administrator
RDML Tim Gallaudet, Ph.D., USN Ret

Abstract

DCNet is a research program established by NOAA for the National Capital Region (NCR) as a response to potential threats following the September 11, 2001 attacks on the U.S. Initial goals of DCNet were to explore variations in model inputs for both numerical weather prediction (NWP) as well as atmospheric transport and dispersion models (AT&D), how to assimilate urban observations into both NWP and AT&D models, and the provision of real-time meteorological observations over the greater NCR to support current numerical weather prediction models as well as provide the driving meteorological observations for atmospheric transport and dispersion models. The DCNet data relate to a large urban complex covering a broad spectrum of weather conditions, permitting an unparalleled description of the atmospheric flow behavior over a complex urban area largely unaffected by major terrain inconsistencies. The network collected standard meteorological data and measurement of characteristics of atmospheric turbulence at 16 locations; only one DCNet (U.S. Department of Commerce Herbert C. Hoover Building, USDOC HCHB) site within the NCR is currently active. HCHB was installed in 2003; HCHB has a primary (Hoover-North) and secondary (Hoover-South) monitoring station. Data archiving began in 2004.

Utilization of atmospheric measurements requires both a description of the acquired observations plus a discussion of the representativeness of those observations. This report provides a description and a brief analysis of both mean and turbulence observations of the DCNet HCHB Hoover-North monitoring station for the period 2017-2019. Comparison of mean wind and temperature observations against regional NOAA National Weather Service monitoring sites is provided as reference for the HCHB observations. Total kinetic energy (TKE) is calculated from the horizontal and vertical turbulence statistics u'^2, v'^2, w'^2. Turbulence measurements are compared to well-accepted atmospheric boundary-layer values proposed by Garratt (1992). Furthermore, the mean stability term (z/L) is calculated based on Monin-Obukhov Similarity Theory. Overall, this data analysis is an important step to providing a foundation for the use of DCNet research network in order to improve the formulations of key variables controlling dispersion model calculations in urban areas, such as Washington, D.C.

Contents

List of Figures

List of Tables

1.0 Introduction

DCNet is a research program established by NOAA for the National Capital Region (NCR) as a response to potential threats following the September 11, 2001 attacks on the U.S. As a spatially and temporally high-resolution meteorological network in the NCR, DCNet was developed to support improvement of urban monitoring methodologies (Hicks, 2005). The goal of DCNet has been the provision of real-time meteorological observations over the greater NCR to support development of numerical weather prediction models as well as provide the driving meteorological observations for atmospheric transport and dispersion models (Hicks et al., 2012), such as the HYSPLIT (Hybrid Single-Particle Lagrangian Integrated Trajectory) model (Draxler and Hess 1997; Stein et al., 2015) developed by NOAA ARL (National Oceanic and Atmospheric Administration Air Resources Laboratory). Additionally, observations have served as a rich observational database of mean values and turbulence supporting the development of the next generation hazard assessment tools.

Discussions within NOAA questioned what sort of atmospheric monitoring network was needed for the NCR, the original concept called for 100+ monitoring stations to cover the roughly 500 km^2 of the NCR. The envisioned extensive network of surface-based meteorological stations and boundary-layer monitoring was designed to address potential chemical, biological, radiological and nuclear threat analyses that would allow emergency managers and first responders to make timely and effective decisions.

The design of the DCNet monitoring network was based on a tiered weather monitoring approach which recognized that multiple levels of meteorological monitoring were required to address dispersion predictions for a wide range of nuclear, biological radiological and chemical (NBRC) potential airborne threats to the NCR. It was simply not economically nor logistically feasible to install and maintain the initially proposed extensive (100+ station) surface-based atmospheric turbulence network for the NCR. A viable alternative approach was proposed to utilize the complex network of private meteorological monitoring stations, to explore the utility of using local meteorological data from private as well as government sources in forecasting for urban areas (Pendergrass et al., 2010). For example, WeatherBug (originally a component of AWS or Earth Works, now GroundTruth [xAd]) provides routine monitoring data from dozens of school systems across the region (see http://weather.weatherbug.com). The surrounding states of Maryland and Virginia, offer a limited set of meteorological observations from highway systems and environmental compliance networks. NOAA's Meteorological Assimilation Data Ingest System (MADIS) program captures much of the available information to support daily weather forecasts.

While there is a wide range of weather monitoring capability within the region, not all weather monitoring can provide appropriate support for atmospheric transport and dispersion. Within WMO's guidance for meteorological instruments and methods of observation (WMO, 2008), the

first requirement is site representativeness. Primary importance is placed on defining the reference scale for the observations; whether micro (less than 100 m), local scale (100m to 3 km), or mesoscale (3 km to 100 km). For example, State and local transportation (highway) systems are designed to monitor the micro-scale associated with road conditions; Weatherbug school systems installed above the school roofs represent local-scales. In these examples, incorporating weather data from stations with multiple scales associated with instrument siting, without through analyses defining how to extract relevant dispersion statistical measures, can lead to misleading conclusions with respect to atmospheric dispersion. However, the data provide a rich background of atmospheric information to supplement the detailed intensive measurements of DCNet.

The focus of DCNet is "dispersion meteorology"; in this application it is predicting the transport and dispersion of chemical, biological, radiological and nuclear materials within complex environment of the urban environment. Given the state-of-the-science of urban numerical consequence assessment capabilities at the time of the September 11, 2001 attacks, and perhaps even today, the best approach to support dispersion meteorology has been provision of accurate and timely model input data through extensive meteorological monitoring. Operationally, the detailed numerical weather prediction models which drive state-of-the-science dispersion models such as HYSPLIT provide 12 km gridded output. For the NCR, this results in roughly 2 or 3 model grid points within the central NCR urban core on which to forecast transport and dispersion. Numerical weather predictions from the NOAA National Weather Service (NWS) models are at a larger grid size and do not make use of observations within the urban core. Instead, they are based on micrometeorological data gathered up to tens of kilometers away from the urban area in question. Their weather-forecasting purpose ordains that their intended application is sufficiently above the surface roughness layer where people live and work (Hicks et al., 2013).

For the NCR, NWS meteorological stations located at the regional major airports provide meteorological information representative of environments considerably different from downtown NCR urban core. NWS weather monitoring is designed to provide the best possible guidance for aircraft operations, but the DCA observations are often not relevant to the dispersion regime of the central part of the NCR. Even higher resolution NWS models, such as the 3 km High Resolution Rapid Refresh (HRRR) Model (Glahn et al., 2017), are influenced by the site-specificity of the routinely-collected NWS data. Programs, like DCNet, provide a sound basis for improving descriptions of wind fields within the NCR and for producing dispersion assessments that correctly account for the changing surface of the area (Callahan et al., 2008).

Urban environments present numerous challenges to predicting potential street level exposures to releases of hazardous materials. As indicated in the previous discussion, operational numerical weather prediction models have very limited, or no, information about the underlying urban environment. Since NWP model scales do not allow for incorporation of the urban topology, addressing the increased turbulence imposed by building, etc. is accomplished through changing

the underlying surface roughness effectively slowing and redirecting the local flow as well as increasing the level of turbulent mixing (Baklanov et al., 2018).

The National Urban Data and Access Portal Tool (NUDAPT) provides basic urban parameterization values for buildings including plan and frontal areas as well as the estimated increased surface roughness (Ching, 2009). Surface roughness values are tied to ratios of plan area (λ_p) and frontal areas (λ_f). Again, this only provides a methodology to address the overall flow structure, and it does not apply to the urban street canyon. For those urban areas where structure heights are well controlled and building densities provide relatively large plan ratios, atmospheric flows tend to separate regimes where the highly three-dimensional chaotic flow within street canyons tends to be decoupled from flow conditions above the urban rooftops (the so-called "skimming" flow).

The NCR was selected as the focal area because of: (i) its known status as a target for terrorist attack, (ii) its history as a site for research using atmospheric tracers (Draxler, 1987a, b; Draxler, 2006), and (iii) the unusually confined building dimensions (with building heights not exceeding about 27 m as required by the Washington Building Act of 1910). Even beyond the urban core, the NCR is "well behaved" (Figure 1, note λ_f and λ_p for the NCR). Remember that it is not only the buildings that cause urban turbulence; the NCR is well forested. The urban environment presents a dense surface structure to the over-lying atmospheric flow. The NCR provides a case of skimming flow where the assumptions of horizontal homogeneity and stationarity apply (Hicks et al., 2009).

The NCR experience is not unlike the dense urban areas of Los Angeles. Beyond the urban core; the LA urban area is dominated by one-or-two story closely packed areas. The NCR offers a tractable testbed for addressing the complex flow structure of the urban environment. As illustrated in Figure 1, the NCR falls within a defined skimming flow regime. From a modeling and analysis perspective, the urban area can be divided into the atmosphere above the tops of the local building configuration and the flow within the complexity of the urban street canyon. Skimming flow is characterized, much like a forest, with the intermittent transfer of energy and mass between the over-riding atmosphere with the chaotic flow of the street canyon.

The DCNet urban data are unique because they cover many years at many locations. They relate to a large city during all weather and climatic conditions, permitting an unparalleled description of the atmospheric flow behavior over a complex urban area largely unaffected by major terrain inconsistencies (Hicks et al., 2012). This report only describes the installation of the two DCNet stations on the USDOC H.C. Hoover (HCHB) building. Within the network, these two sites are referenced as Hoover-North (primary) and Hoover-South (secondary). For this report, the HCHB Hoover-North (hereafter simply referenced as Hoover) database will be explored.

Chapter two provides a detailed description of siting, instrumentation, and data logistics associated with the Hoover measurement systems. Chapter three provides illustrations of the standard meteorological data and the characteristics of atmospheric turbulence. Chapter four

provides an analysis of mean and turbulent wind and temperature measurements with a comparison to regional NWS measurement sites and accepted micrometeorological measures to document the representativeness of the DCNet Hoover observations.

2.0 Hoover Station Design

At its largest configuration, the DCNet network collected standard meteorological data and measurement of characteristics of atmospheric turbulence at 16 locations (Figure 2). Station locations were designed to maximize interoperability with available private weather networks. Only one DCNet site within the NCR is currently active (DC001, DC002) as of 2020 (Table 1).

For logistical support, there was one standard design for all DCNet stations sensors, installation hardware, data acquisition software and communications hardware. Only the physical installation and support structure, was modified to meet site specific requirements.

This report focuses on the description of the DCNet core observation site on the rooftop of the US Department of Commerce, Herbert Building, 1401 Constitution Avenue, Northwest, Washington, DC (38.894^0N, 77.033^0W). Two monitoring stations (a primary and backup) are installed at this site. Monitoring towers are sited to provide 10 m observations above the zero-plane displacement referenced to the HCHB rooftop. Observations of winds and temperature are 10 m above the top of the roof (Figure 3). USDOC HCHB Hoover-North station (Hoover) was installed in 2003 with data archiving began in 2004. This operated continuously from 2003 to 2010 when the station was dismantled to facilitate installation of a new roof for the HCHB building. The site was maintained intermittently after 2012 until 2016 when the monitoring station was refurbished. This site served as the central point within the NCR, and it is on a multistory building that occupies most of a city block but that is similar in height to most of its neighbors.

This DCNet site includes sonic anemometers installed on top of meteorological tower mounted 10 m above the rooftops of the HCHB building (Figure 4). The meteorological tower also included instruments to measure air temperate, relative humidity and net radiation. All of these variables were measured at high temporal frequency (10 Hz). Data included in this analysis covers only the period between 2017 and 2019.

2.1 Instrumentation

A heavy-duty tower (C-33, 10 m, Climatronics Corporation, Bohemia, NY) was mounted above the rooftops of the Hoover building. The meteorological tower is equipped with a sonic anemometer (RM Young model 81000V) and a wind vane propeller (RM Young model 05305).

The tower also includes instruments to measure air temperate, relative humidity and net radiation. The specifications of temperature and solar radiation sensors are shown in Table 2. A Campbell scientific datalogger (CR1000) is used for data acquisition and measurement control.

2.2 Data Acquisition and communications

DCNet data are recorded at a rate of 10 Hz then reported as 15 min averages. Initial communications were provided through a dedicated RF Radio network at 170.2 Mhz; this communication system was replaced with dedicated Cellular modems. Note that the Campbell Scientific software is able to identify the station by dedicated IP address.

2.3 Data processing and archiving

DCNet data collected and/or recorded and products generated are managed by Air Resources Laboratory (ARL) and the principle investigator (PI) and are archived on secure computing systems at Atmospheric Turbulence and Diffusion Division (ATDD). All data recorded, products generated, and discoveries made during experimental studies will be made discoverable and accessible to the general public after quality assurance (QA) and quality control (QC). Public access of these data is achieved through secure FTP servers, public access websites, and customized applications.

Acquired 15-minute averaged observations were stored on the Campbell scientific datalogger (CR1000, Campbell Scientific, Inc., Logan, UT). Running means and cross-products were carried out within the data acquisition process. Due to the limited computing speed on the CR1000 datalogger to both acquire and process data, the post-processing step began by using software to provide an initial level of quality control and particularly to perform the coordinate transformation.

Large errors have been reported by several researchers in evaluating fluxes because of the inappropriate orientation of the vertical sensors due to the non-simple terrain and non-stationarity. Therefore, the central consideration to assess turbulent fluxes is the alignment of the anemometers with the average wind vector. Based on the coordinate-rotation scheme developed by Wesely (1970), McMillen (1988) adapted, at the Atmospheric Turbulence and Diffusion Division (ATDD) of the NOAA ARL, located in Oak Ridge, Tennessee, a coordinate transformation technique routinely used in order to rotate the instrumentation coordinate system to ensure that the average vertical wind speed $\overline{w}$ is zero, with the implicit assumption that the fast-response fluctuations in velocity are also appropriately corrected. The software was also used to calculate turbulence variables, such as the friction velocity (u_*), and stability variables, such as the stability parameter (z/L). Acquired data were reported in a CSV file format. The CSV file contains the mean values of the meteorological data (wind speed, wind direction,

temperature, relative humidity, solar radiation) and turbulence data (u_*, TKE, z/L) including the applied coordinate transformation.

3.0 Observations

Long term unattended meteorological monitoring is not a simple process. Power outages, severe weather events, animals, transmission interference are just a few of the many interruptions to the process of data acquisition. For the rooftop operation on the Department of Commerce's Hoover building, there is the additional impediment from the perspective of Secret Service controlled access to the HCHB rooftop and maintenance from a remote NOAA/ARL field division. This section provides a description of the acquired meteorological data and identification of outliers. For clarity, only observations for the period 2017 – 2019 will be presented. Maintenance and oversight of the DCNet system became intermittent after 2010; the monitoring system was slowly dismantled with limited maintenance performed on the urban core DCNet. With the 2016 Presidential inauguration, the core DCNet stations were reconditioned. The 2017-2019 dataset represents the latest period of qualified measurements from the HCHB observation system. As stated above, for this report DCNet DC002 HCHB Hoover-North will be presented; this dataset represents the most complete set of observations from the 2017 – 2019 period.

3.1 Mean observations

3.1.1 Wind Speed

Figure 5 is a time-history plot of wind speed measured on the Hoover monitoring station for the period January 1, 2017 through December 31, 2019. As indicated above, only data from January, 2017 through December, 2019 are plotted; every tenth data point is displayed. Time is local Eastern Standard Time (EST).

Seasonal variation in the mean wind speed is represented in Table 3. For this statistical summary, mean 15-minute averaged winds were scanned to eliminate outliers. To limit extreme wind speeds attributable to performance issues of the sonic anemometers, velocity data were rejected when (1) the horizontal variance (u'^2) after coordinate rotation exceeded 10 m/s, (2) when the horizontal variance was less than 0.01 m/s, and (3) when the standard deviation of u, v, or w wind components was zero for the 15-minute observation and averaging period. Velocity data were further restricted to measurements less than 15.0 m/s. The lower wind speed limit was set at 0.25 m/s which is based on the manufacturer published lowest measurement range. The data set was additionally scanned for contiguous, in time, wind speeds or directions; this often occurred during low temperature and high humidity when ice developed on the sonic transducers. Establishing an outlier identification based on horizontal variance excluded less than 0.5% of the wind speed observations; a histogram of accepted mean wind speeds is included in Figure 5.

While there is some variation by season, the overall mean wind speed of 3.0 m/s and standard deviation of 1.5 m/s is quite representative of the observations from the Hoover station. Column 7 of Table 3 provides the geometric mean for each season and all data. The geometric mean is a better reflection of the lognormal distribution of wind speeds shown in Figure 5.

3.1.2 Wind Direction

The dominance of winds from the southwest to northwest is clearly evident in the time-series plot (Figure 6) of wind direction. Rejected wind directions are based on the previously discussed outlier identification process for mean wind speeds addressed in Section 3.1.1. An additional rejection process removed wind directions of 0.0 degrees which was a indicator of ice formation on the sonic anemometer transducers.

Unfortunately, interpretation of potential dominate wind directions from Figure 6 is quite difficult due to the large number of data points, even with a reduced plot displaying every tenth point. Figure 7 plots wind speed versus wind direction for all data-hours in the 2017-2019 dataset. Again, for clarity only every tenth data point is displayed. As shown, highest wind speeds are associated with winds from the northwest. The trimodal nature of wind directions (northeast, southwest, and northwest is clearly evident in Figure 7. As expected, this analysis reflects the overall impact of synoptic scale weather systems impacting on the National Capital Region as well as influence for regional topographical features such as the Potomac and Anacostia Rivers.

3.1.3 Ambient Temperature

Observations of ambient temperature for the Hoover site are presented in Figure 8. Monthly means and extremes for the 2017 – 2019 time period are tabulated in Table 4. For this analysis, measured temperatures were restricted to observations greater than -15 ^{0}C and less than +42 ^{0}C and the dataset was scanned for conditions where contiguous 15-minute means were constant.

The column mark morning low is the mean low temperature between 1:00 and 5:00 am EST; daytime high is the mean high temperature between 13:00 and 17:00 hours. The last column in the table is the climatological monthly average based on 6 years of DCNet HCHB observations from 2004 – 2010. The selected dataset used in this NOAA Technical Memorandum appears representative of the climatological monthly averages.

3.2 Turbulence observations

A key component of DCNet was the acquisition of both mean and turbulence statistics for the Hoover station as well as the full DCNet network. Horizontal and vertical turbulence define the spread of hazardous materials in the atmosphere. As described in the HYSPLIT Lagrangian

model description (Draxler, 1997), a turbulent component is added to the mean advection to obtain a new particle position as (Eq. 56/Eq. 57)

$$X_{final}(t + \Delta t) = X_{mean}(t + \Delta t) + U'(t + \Delta t)\Delta t G$$

$$Z_{final}(t + \Delta t) = Z_{mean}(t + \Delta t) + W'(t + \Delta t)\Delta t G$$

Where U' and W' are the horizontal and vertical velocity components

As described in the previous section, a conservative outlier rejection process was applied to the turbulence measurements. Selected rejection cut-points are discussed for each of the follow turbulent parameters. Applying the selected outlier identification results in marking less than 0.5% as questionable. A more aggressive process of outlier identification does not significantly alter the analysis of variable means suggesting a random occurrence of extremes.

The large apparent variability in turbulence statistics (Figures 9,10, and 11) is a consequence of the averaging period. The 15-minute averaging period for turbulence was a compromise between obtaining mean wind and temperature observations to support emergency management requirements and obtaining representative velocity variances. While perhaps desirable, longer sampling and averaging time were restricted by data acquisition and process capabilities of the station datalogger.

3.2.1 Horizontal and vertical velocity variances

Figures 9, 10 and 11 plot time series of horizontal and vertical velocity variances (u'^2, v'^2 and w'^2) measured based on technique previously detailed in section 2.3 with the coordinate transformation applied. Included with each plot is a histogram of measured variances based on the outlier identification process. For all three turbulence variances, a minimum level was set at 0.01 m^2/s^2. Velocity variances were rejected for u'^2 >10.0 m^2/s^2, v'^2 >7.0 m^2/s^2, and w'^2 > 1.5 m^2/s^2. As illustrated in supplied histogram of measured variances, the outlier rejections process was quite conservative; this process simply rejected the far extremes of each variance distribution.

Figure 12 plots the hourly mean horizontal and vertical velocity variances for the 2017 – 2019 dataset. The hourly averaged variances appear quite consistent and do not show significant excursions across the 24-hour period. The near constant value across the nighttime period, increase with onset of sunrise, daytime mid-afternoon peak, and slow decrease with evening transition are quite typical of diurnal variation in atmospheric turbulence.

3.2.2 Shear Stress

Figure 13 plots a time series of shear stress (or u_*) for the Hoover monitoring station. As previous, a histogram is included to demonstrate the limited impact of applying the outlier identification process on the distribution of observations. In this case, measurements of u_* were limited to observations greater than 0.01 m/s and less than 1.5 m/s.

The dataset mean u_* is 0.4 m/s.

3.2.3 Sensible Heat Flux

Figure 14 plots the time series of acquired sensible heat flux. Observations of $\overline{w'T'}$ have been scaled with density and heat capacity to obtain units of watts/m^2. As with previous measurements, a histogram has been added to document the spread of Heat flux measurements after a lower outlier bound of -150 watts/m^2 and upper bound of 350 watts/m^2 have been applied. Eliminating observations outside of these bounds has little impact on calculation of means. Note that, with the exception of the latter months of 2019, the measured heat flux rarely falls below zero. It should be recognized that, in the same manner that the forest floor and canopy contribute to the measured heat flux, Hoover measurements of heat reflect the anthropogenic contribution from the rooftop surface of the HCHB complex and operating environment of HCHB contributing to the heat transfer to the roof surface.

4.0 Data Evaluation

Section 4 provides a brief analysis of mean and turbulent wind and temperature observations demonstrating the representativeness of the Hoover measurements. Comparison of mean wind and temperature observations against regional National Weather Service monitoring sites is provided as reference for the Hoover mean wind speed, wind direction, and temperature observations. Turbulence measurements are compared to well-accepted atmospheric boundary-layer values developed by Garratt (1992).

4.1 Mean Wind and Temperature

Figure 15 provides a set of wind rose (joint wind speed and wind direction frequencies) plots of the 2017-2019 Hoover 15-minute mean wind observations. Seasons are defined as January – March (Winter), April – June (Spring), July – September (Summer) and October – December (Fall). The dominant southerly and northwestly wind directions are quite apparent. As previously shown in Figure 7, highest wind speeds are associated with northwesterly winds.

Comparison of the regional climatological wind is provided in Figure 16. In addition to the Hoover site, joint wind speed and wind direction distributions are plotted for two regional NWS stations (DCA and IAD). NWS station DCA (Ronald Reagan National Airport) is located approximately 5 kilometers south of the HCHB complex. NWS station IAD (Dulles International Airport) is located roughly 35 km northwest of the HCHB complex. In general, the three stations are quite comparable. All three sites show the dominate northwestly and southerly winds attributed to the passage of synoptic scale weather systems. Northeasterly winds measured at DCA and Hoover both reflect the influence of the Potomac and Anacostia Rivers.

Figure 17 plots a simple linear regression of DCA and IAD measured wind speeds against Hoover observations; the linear fits indicate similar agreements and correlation with mean winds although there is considerably more variability between Hoover and IAD wind speeds. Based on the simple linear regression, central urban wind speeds are roughly 75% of the non-urban areas. At the level of the mean Hoover wind speed (3.0 m/s), the Hoover wind speed is roughly 1 m/s slower than DCA and IAD.

Results of a simple linear regression of ambient temperature measured at IAD and DCA against Hoover's observations are given in Figure 18. As with the wind speed correlation there is general agreement (large R^2) between measured mean ambient temperatures between Hoover and the two regional NWS stations, DCA and IAD. There is clearly more variability associated with the regression between Hoover and IAD. Figure 19 explores this variability with a comparison of the mean temperature difference between the two regional NWS stations and the Hoover observations. Graphed in Figure 19 is the mean temperature difference (defined as Hoover minus NWS station) as a function of hour (EST) of the day. Both plots show a decided diurnal pattern with mean temperature differences near +0.5 degrees at night and -0.5 degrees during the day for DCA and near +3.0 degrees at night and +0.5 degrees during the day for IAD. The IAD comparison provides an indicator of the heat-island effect where the consolidated urban core is significantly warmer than the surrounding suburban/urban areas. This is readily evident during the night attributed to building thermal storage associated with the NCR central urban area.

4.2 Turbulence Statistics

Confidence in the turbulent wind and temperature data comes through a comparison of Hoover measured and calculated turbulence parameters against well accepted values defined in the atmospheric literature. In particular, within this section, Hoover measured and calculated values will be compared to the suggested values of Garratt (1992),

$$\text{TKE}/u_*^2 = 5.46,$$
$$u'^2/u_*^2 = 5.76,$$
$$v'^2/u_*^2 = 3.61, \text{ and}$$
$$w'^2/u_*^2 = 1.56.$$

Confirmation of Hoover shear stress (u_*) measurements comes indirectly through evaluation of the normalized shear stress using the mean wind speed; defined as the friction coefficient (cf). Figure 20a provides a regression analysis of wind speed (u) versus u_*, the coefficient of 0.13 is within bounds of accepted values ranging from 0.1 to 0.14 depending on surface type (Hicks et al., 2014). Figure 20b plots Hoover friction coefficient as function of hour of the day; while there appears to be some variability between nighttime and daytime conditions, diurnal differences are small and well within uncertainty bounds.

Figure 21 plots measured sensible heat flux (H) for the Hoover station; the variability in measured sensible heat flux is both a reflection of natural variability and the reduced averaging period selected for DCNet as discussed in the previous Section. The red curve is the mean heat flux binned by hour. It is interesting that while observations show stable conditions during late evening and early morning periods, the mean heat flux for the HCHB building never goes stable.

From the measured shear stress (u_*) and heat flux (H), the stability (z/L) associated with the Hoover monitoring station can be calculated based on Monin-Obukhov Similarity Theory (MOST). The height, z, is the measurement height above the height of the zero-plane displacement and L is defined as

$$L = u_*^3 \bar{\theta}_v / kg(\overline{w'\theta_v'}).$$

Figure 22 plots a histogram of M-O stability (z/L) for the Hoover monitoring station using the observed shear stress, heat flux and temperature as defined in the above equation. Figure 22 provides a binning of calculated stability (z/L) indicating near neutral conditions (+/- 0.2) for almost 80% of the monitoring hours; The near neutral conditions for the Hoover site are highlighted in Figure 23. Across much of the diurnal cycle, the mean stability term (z/L), as plotted in Figure 24, is near zero indicating neutral to slightly unstable conditions.

The assumption of near neutral atmospheric stability for the Hoover station provides the framework for evaluating measured turbulence statistics against the accepted values provided by Garratt (1992).

Figure 25 plots the calculated total kinetic energy (TKE, with the role of air density ignored as is common in relevant literature) from the horizontal and vertical turbulence statistics u'², v'², w'² in the form

$$TKE = 0.5 * (u'^2 + v'^2 + w'^2).$$

Graphed variables of TKE have been limited based on the previously described outlier identification process.

Following the formulation presented in Garratt, Figure 26 (all observations) and 27 (day/night separation) provide regression analyses of calculated TKE versus measured shear stress. Figures 28,29, and 30 present regression analyses of turbulence statistics and TKE for u'², v'², and w'²

respectively. Slopes from the individual regression analyzes are tabulated in Table 5. The larger values of TKE and variances are simply a reflected of the increased turbulence associated with the urban environment. However as shown in Table 6, the relative contribution of individual turbulence components is quite comparable to that proposed by Garratt (1992).

5.0 Summary

This report presents a description and a brief analysis of the standard meteorological data and the characteristics of atmospheric turbulence of the DCNet Hoover-North station for the period 2017-2019. These data are unique because they are gathered within the urban core with sufficient sensors to describe all of the motions that are controlling local dispersion. A key component of DCNet is the acquisition of both mean and turbulence observations, these observations were scanned to eliminate outliers. The method of outlier identification resulted in loss of less than 0.5% of the overall data. Seasonal wind roses showed that highest wind speeds are associated with winds from the northwest and the south. This analysis reflects the overall synoptic scale weather systems impacting on the NCR as well as influence for regional topographical features such as the Potomac and Anacostia Rivers. The comparison of mean wind and temperature data for the Hoover observations against regional NWS monitoring sites enabled the demonstration of the representativeness of the Hoover measurements. The calculated TKE from the horizontal and vertical turbulence statistics u'^2, v'^2, w'^2 showed large values reflecting the increased turbulence associated with the urban environment. However, the relative contribution of individual turbulence components is quite comparable to the suggested values of Garratt (1992). Furthermore, the mean stability term (z/L) calculated based on Monin-Obukhov Similarity Theory indicated near neutral conditions for almost 80% of the monitoring hours.

In the future, analysis of the measurements and findings from the DCNet research network will be used to improve the current parameterizations of key variables controlling dispersion model calculations in urban areas, such as Washington, D.C. The next step will be to compare DCNet data against predictions from meteorological models of the National Weather Service, such as the High Resolution Rapid Refresh (HRRR) model, the North American Mesoscale (NAM) model, and the Finite Volume Cubed-Sphere dynamical core (FV3) to produce modifications of the approximation techniques which control dispersion model calculations and subsequent impact predictions. The proposed adjustments will be evaluated for implemented in current complex atmospheric transport and dispersion models such as NOAA/ARL's HYSPLIT predictive system. This effort will open perspectives towards understanding the complexities of modeling the atmospheric dispersion process for other urban environments.

6.0 Acknowledgements

7.0 References

Baklanov, A., Grimmond, C.S.B., Carlson, D., Terblanche, D., Tang, X., Bouchet, V., Lee, B., Langendijk, G., Kolli, R.K., Hovsepyan, A., 2018. From urban meteorology, climate and environment research to integrated city services. Urban Climate, 23, 330-341.

Callahan, W., and B. B. Hicks, 2008: Utilizing surface network data in urban dispersion models. Presentation J16.3 of the 89th Annual Meeting of the American Meteorological Society, Phoenix, AZ.

Ching, J., Brown, M, Burian, S. Chen,F, Hanna, A., Hultgren, T., Sailor, D., Taha, H. and Williams, D., 2009. National Urban Database and Access Portal Tool (NUDAPT): Facilitating a new generation of advanced urban meteorology and climate modeling with community-based urban database system. Bulletin of the American Meteorological Society (BAMS), August.

Draxler, R.R., 1987a. One year of tracer dispersion measurements over Washington, D.C. Atmos. Environ, 21, 69-77.

Draxler, 1987b: Accuracy of various diffusion and stability schemes over Washington, DC. Atmos. Environ., 21, 491–499.

Draxler, R.R., and Hess, G. D., 1997. Description of the HYSPLIT_4 modeling system. NOAA Tech. Memo. ERL ARL-224, 24 pp.

Draxler, R.R., 2006. The use of global and mesoscale meteorological model data to predict the transport and dispersion of tracer plumes over Washington, D.C. Wea. Forecasting, 21, 383–394.

Garratt, J. R., The Atmospheric Boundary Layer. University Press, 316 pp

Glahn, B., Schnapp, A.D. Ghirardelli, J.E. and Im, J., 2017. A LAMP–HRRR MELD for Improved Aviation Guidance. Wea. Forecasting, 32, 391–405.

Hicks, B.B., 2005. Urban dispersion for the 21st century. WIT Transactions on The Built Environment, 82: 555-566.

Hicks, B. B., W. R. Pendergrass, C. A. Vogel, and R. S. Artz, 2008: On the coupling between urban surface winds and skimming flow. Presentation J16.1 of the 89th Annual Meeting of the American Meteorological Society, Phoenix, AZ.

Hicks, B. B., Callahan, W. J., Pendergrass III, W. R., Dobosy, R. J. and Novakovskaia, E. 2012. Urban turbulence in space and time. J. Appl. Meteor. Climatol., 51, 205–218.

Hicks, B.B., Novakovskaia, E., Dobosy, R.J., III, W.R.P., Callahan, W.J., 2013. Temporal and Spatial Aspects of Velocity Variance in the Urban Surface Roughness Layer. J. Appl. Meteor. Climatol., 52, 668-681.

Hicks, B. B., W. R. Pendergrass, C. A. Vogel, and R. S. Artz, 2014: On the Drag and Heat of Washington, D.C., and New York City. *J. Appl. Meteor. Climatol.*, **53**, 1454–1470.

McMillen RT (1988) An eddy-correlation technique with extended applicability to non-simple terrain Boundary-Layer Meteorology 43:231-245.

Pendergrass, W.R., C. A. Vogel, B. B. Hicks and W. Callahan, 2010. comparison of co-located DCNet and AWS weatherbug urban temperature observations. Presentation 6.2 of the 90th Annual Meeting of the American Meteorological Society, Atlanta, GA.

Stein, A.F., Draxler, R.R., Rolph, G.D., Stunder, B.J.B., Cohen, M.D., Ngan, F., 2015. NOAA's HYSPLIT atmospheric transport and dispersion modeling system. Bull. Am. Meteorol. Soc. 96, 2059-2077.

Wesely, ML (1970). Eddy correlation measurements in the atmospheric surface layer over agricultural crops. Ph.D. Dissertation, University of Wisconsin.

WMO, 2008. Guide to Meteorological Instruments and methods of Observation, WMO-No.8, World Meteorological Organization, Geneva, Switzerland.

Table 1: Properties of Current (2020) operating DCNet monitoring stations

Site reference: DC001/DC002

Site name: USDOC H.C. Hoover (HCHB) building.

Date of operation: 2003 - present

Latitude (°N): 38.894

Longitude (°W): 77.033

Table 2: DCNet standard monitoring instrumentation

	Temperature and Relative Humidity Probe		Solar Radiation Sensor
	T° Sensor	RH Sensor	
Model	CS500		LI-190SB
Type	1000 Ω PRT, DIN 43760 B	INTERCAP ®	Quantum Sensor
Range	-40°C to + 60°C	0 to 100%	400-700 nm waveband
Accuracy	0 to 10% RH at 20°C		± 5%
Response time	15 sec		10µs

Table 3: Seasonal variation in mean wind speed and standard deviation

Season	Arithmetic Mean (m/s)	Trimmed Mean (m/s)	Standard Deviation (m/s)	Minimum (m/s)	Maximum (m/s)	Geometric Mean (m/s)
January - March	3.45	3.37	1.75	0.288	10.87	3.00
April - June	3.10	3.03	1.47	0.27	10.4	2.74
July - September	2.52	2.48	1.15	0.25	8.97	2.24
October - December	2.93	2.84	1.52	0.27	10.35	2.53
All	3.00	2.91	1.52	0.25	10.87	2.61

Table 4: Monthly mean temperature, standard deviation and extreme measurements.

Month	Average (°C)	Standard Deviation (°C)	Minimum (°C)	Maximum (°C)	Morning Low (°C)	Daytime High (°C)	Climatology (2004-2009)
January	3.92	6.75	-11.96	21.7	2.56	5.83	3.16
February	7.40	6.32	-7.32	27.08	5.53	9.68	3.81
March	7.46	6.01	-5.48	26.8	5.28	10.09	8.75
April	15.6	6.10	0.90	33.1	12.74	18.73	14.69
May	20.68	5.12	8.33	33.47	17.77	23.88	19.05
June	24.67	4.14	13.75	35.31	21.53	27.88	24.24
July	27.24	3.64	17.74	37.39	24.30	30.40	26.08
August	25.98	3.55	16.5	35.72	23.15	29.23	25.94
September	23.37	4.15	12.67	34.97	20.85	26.38	22.05
October	17.60	5.41	4.43	34.78	15.23	20.58	15.95
November	8.78	4.89	-3.09	27.17	6.99	11.25	10.43
December	5.34	4.76	-9.0	19.74	4.08	7.13	5.13

Table 5: Comparison of normalized TKE and horizontal and vertical variances.

	TKE/u_*^2	u'^{2}/u_*^2	v'^{2}/u_*^2	w'^{2}/u_*^2
Garratt	5.46	5.76	3.61	1.56
DCNet Hoover	7.03	7.29	4.67	1.69

Table 6: Relative contribution of horizontal and vertical turbulence to total TKE.

Source	u'^{2}/TKE	v'^{2}/TKE	w'^{2}/TKE
Garratt	1.05	0.66	0.28
DCNet Hoover	1.03	0.66	0.24

Urban Core Morphology		
Parameter	0.25 km² Mean	1.00 km² Mean
Mean Building Height	25.05	17.01
Building Height StdDev	8.57	9.46
λ_P	0.33	0.30
λ_B	1.51	0.91
λ_F 0	0.29	0.16
λ_F 45	0.42	0.22
λ_F 90	0.29	0.15
λ_F 135	0.41	0.22
λ_S	0.58	0.35

Location	Land Use Class	λ_p (0.25km)
Los Angeles, USA	Down Core	0.29
Vancouver, BC	Downtown	0.37
Mexico City, Mexico	Downtown	0.47
National Capital Region	Downtown	0.33

Figure 1: Comparison of plan and frontal area ratios for the NCR and other large urban cores. (λ_F = frontal area, λ_P = plan area.)

DC001	NOAA Hoover Bldg
DC003	National Acad Science
DC004	NOAA Silver Spring
DC005	National Arboretum
DC006	DOE Forrestal
DC008	Frank Reeves Municipal Center
DC009	Navy Annex
DC011	Naval Research Lab
DC012	DC EMA 2
DC013	RFK Stadium
DC014	Ft. A. P. Hill
DC018	National Education Association
DC019	WTOP
DC020	Howard University
DC021	American Geophysical Union
DC023	CSPAN Tower
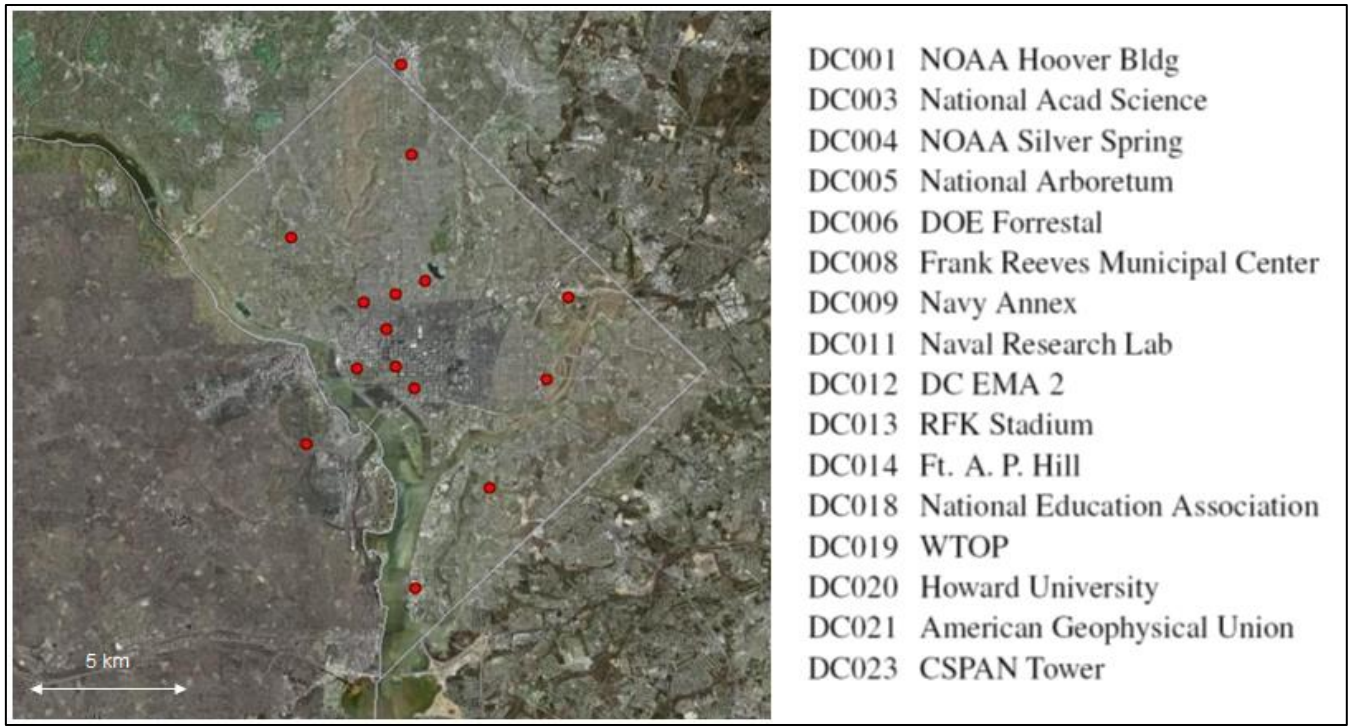
Figure 2: Maximum DCNet monitoring configuration with station identification

Figure 3: Google Earth image of the Department of Commerce Hoover (HCHB) building with station locations highlighted. Photographs show the Hoover-South rooftop monitoring station as installed.
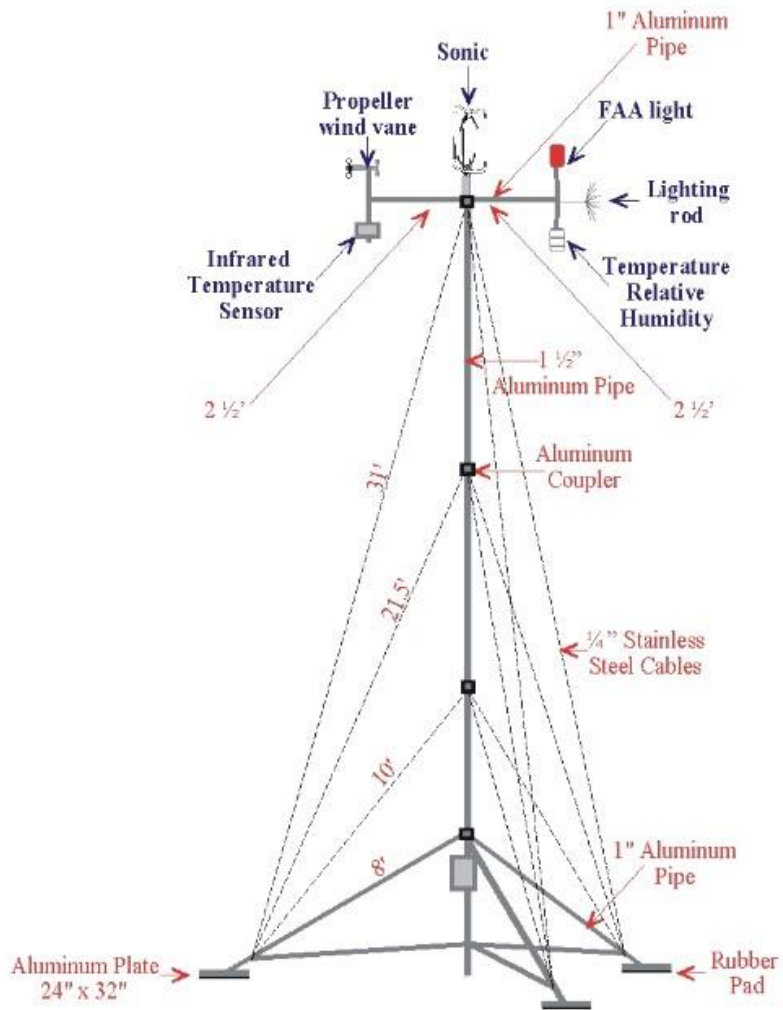
Figure 4: Skematic of DCNet monitoring station. Note that Infrared Temperature sensor was used during ARL's participation in Pasadena urban study as part of NOAA Calnex 2010 program.
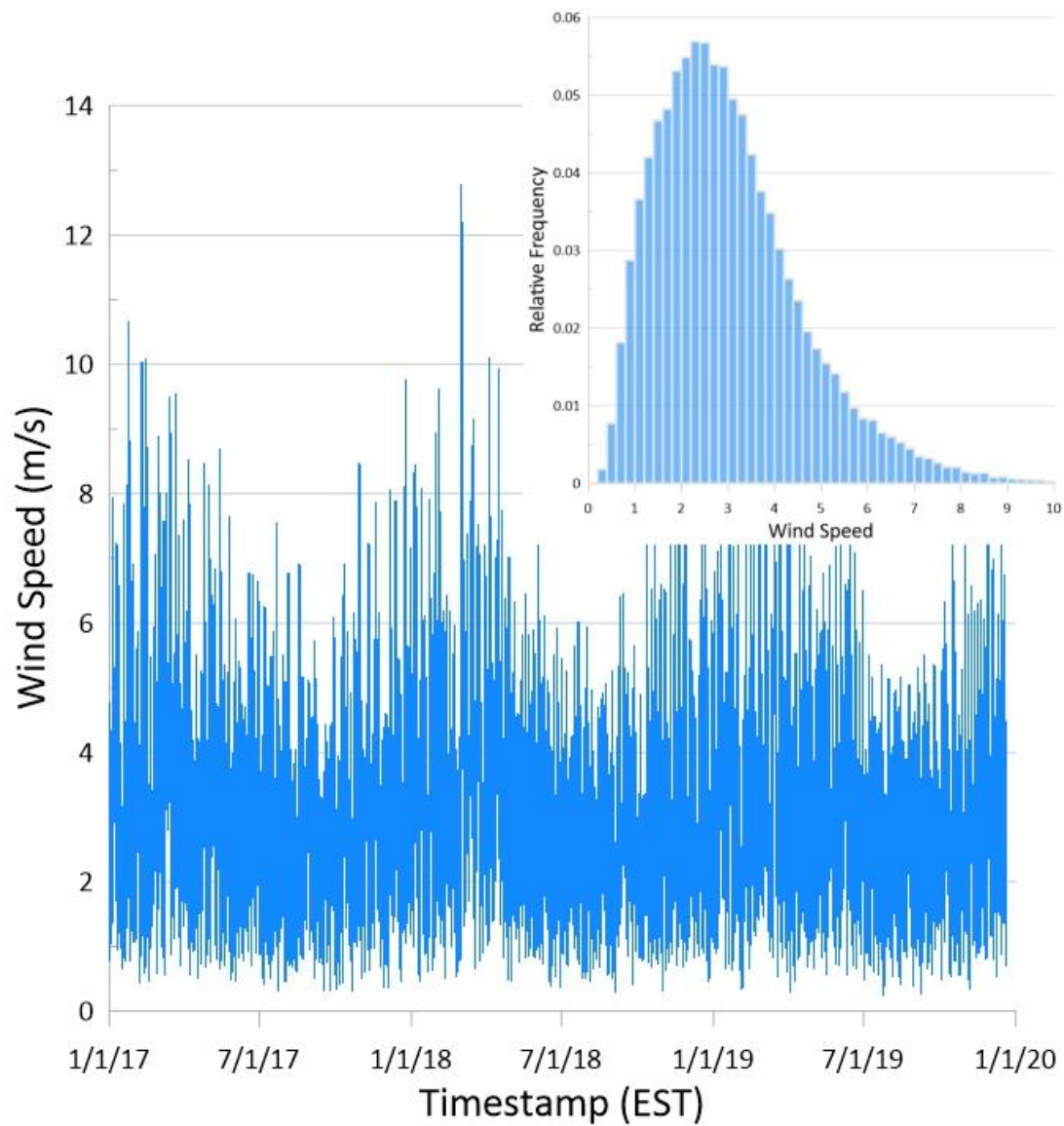
Figure 5: Measured 15-minute average wind speed for the period 1/1/2017 through 12/31/2019. For presentation clarity, every tenth data point displayed. The insert graph provides a histogram of accepted observed wind speeds based on the outlier identification process.
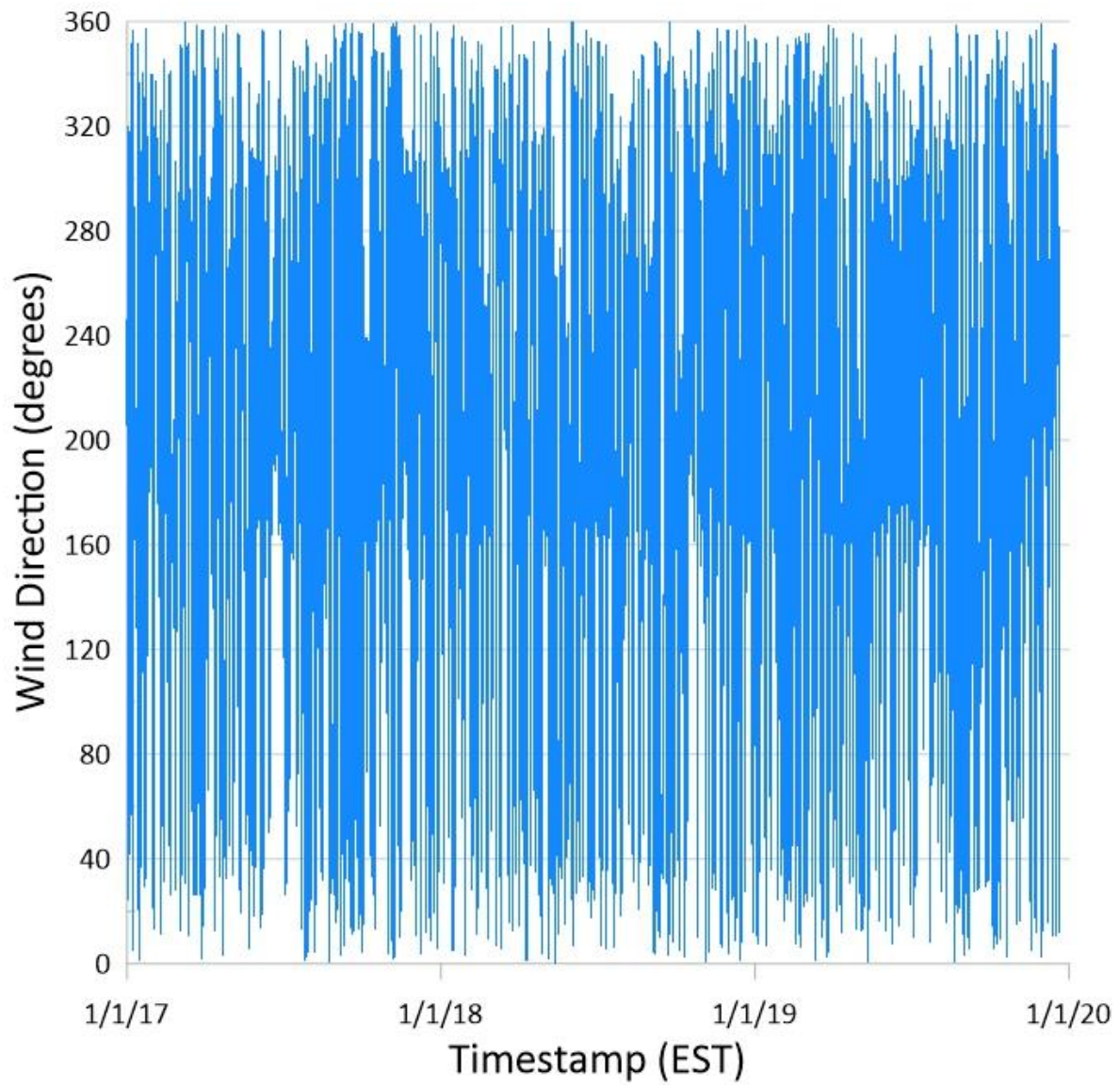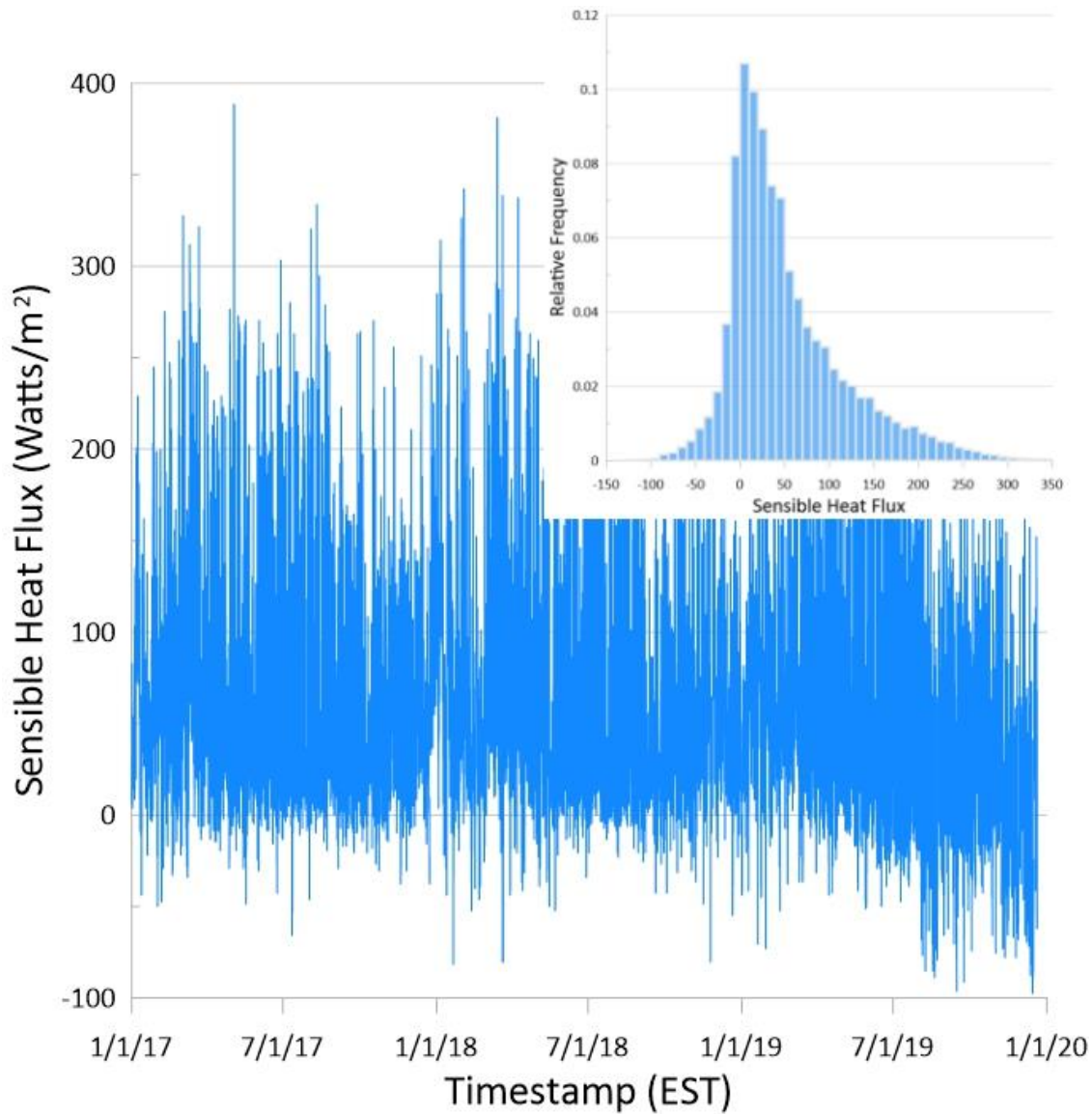
Figure 6: Measured 15-minute average wind direction for the period 1/1/2017 through 12/31/2019. For presentation clarity, every tenth data point is displayed
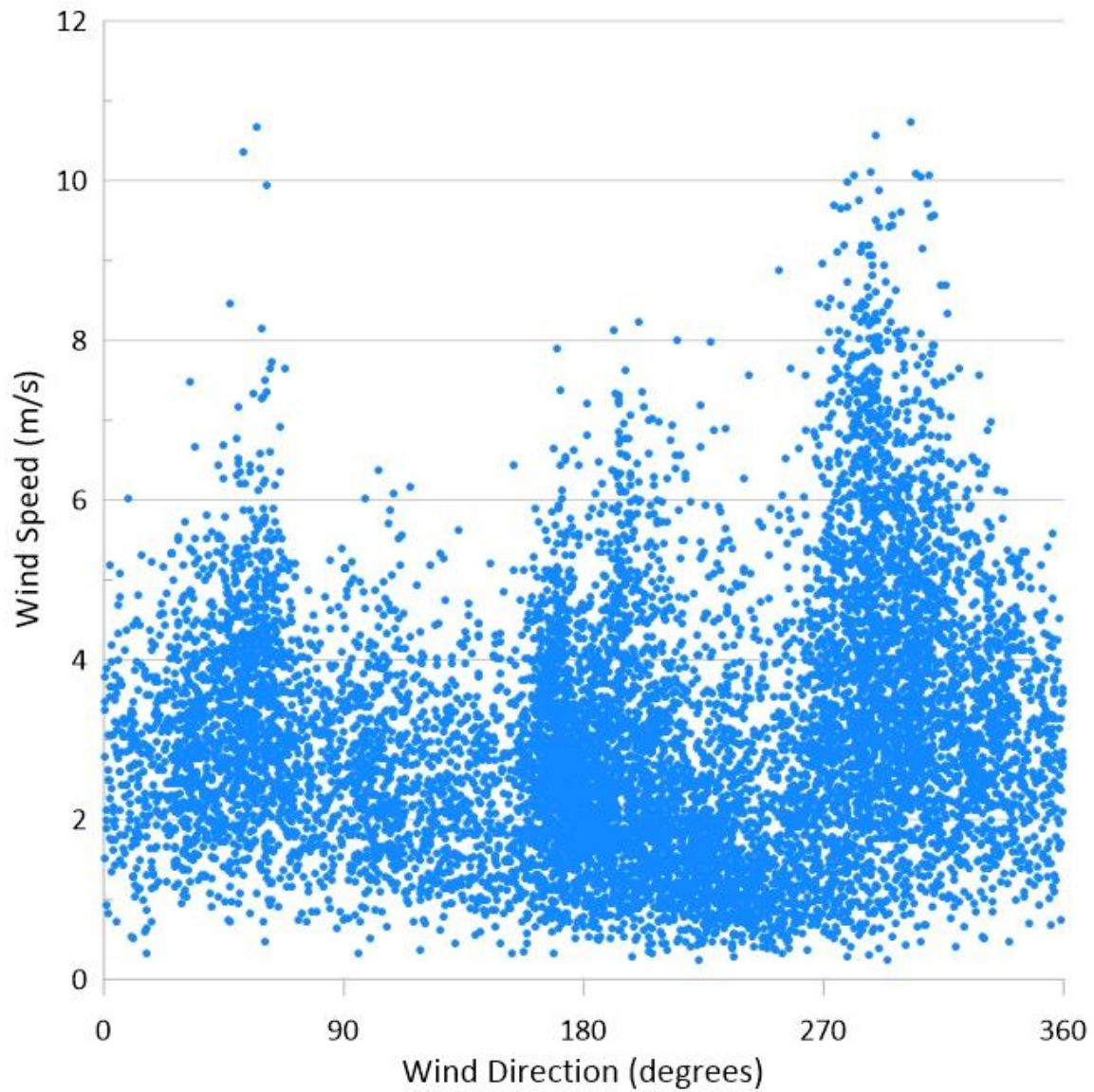
Figure 7: Wind speed versus wind direction for the Hoover station. For presentation clarity, every tenth data point is displayed. The trimodal nature of winds over the Hoover site is quite evident.
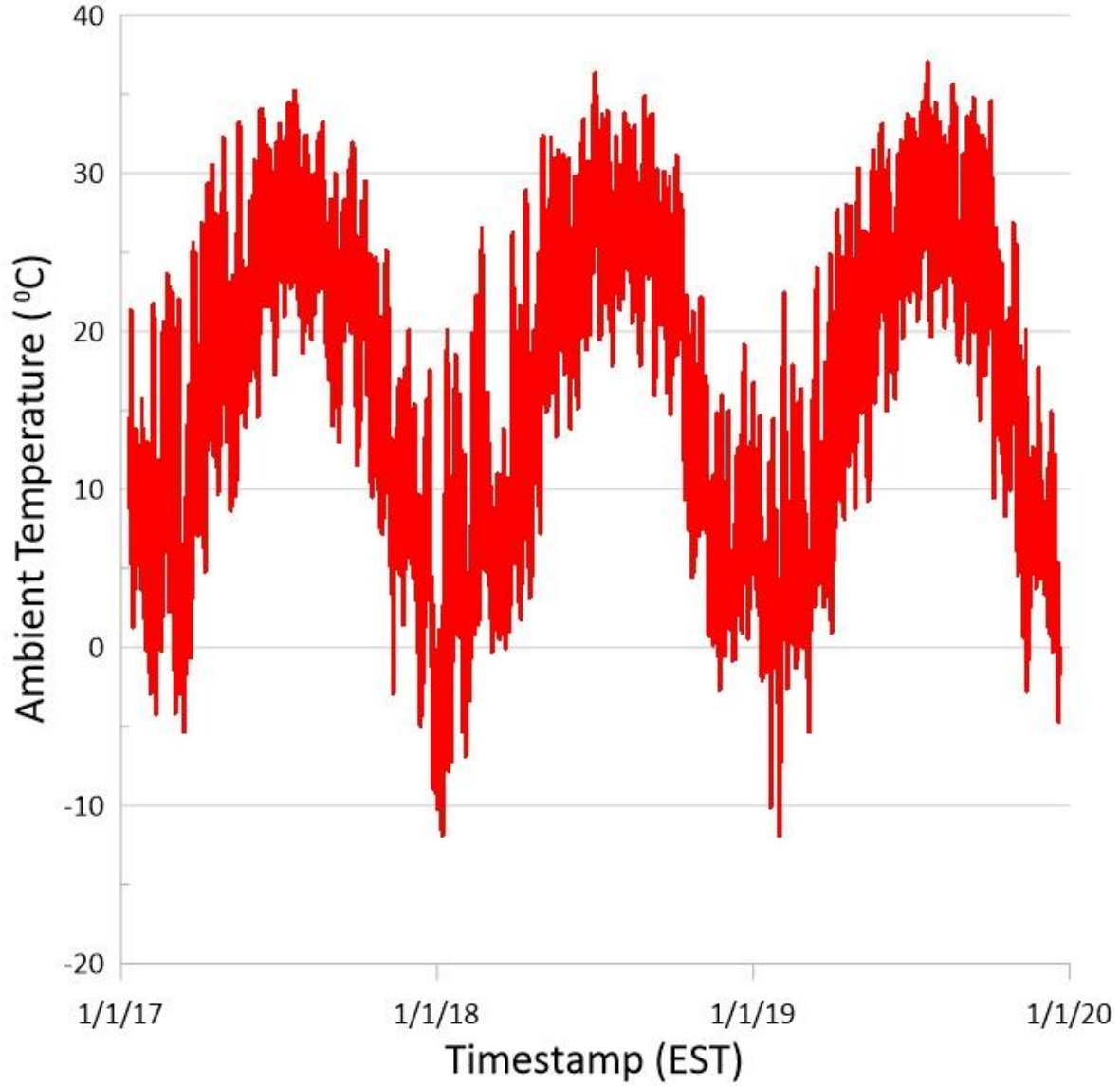
Figure 8: Measured 15-minute average temperature for the period 1/1/2017 through 12/31/2019. For presentation clarity, only every tenth data point is displayed
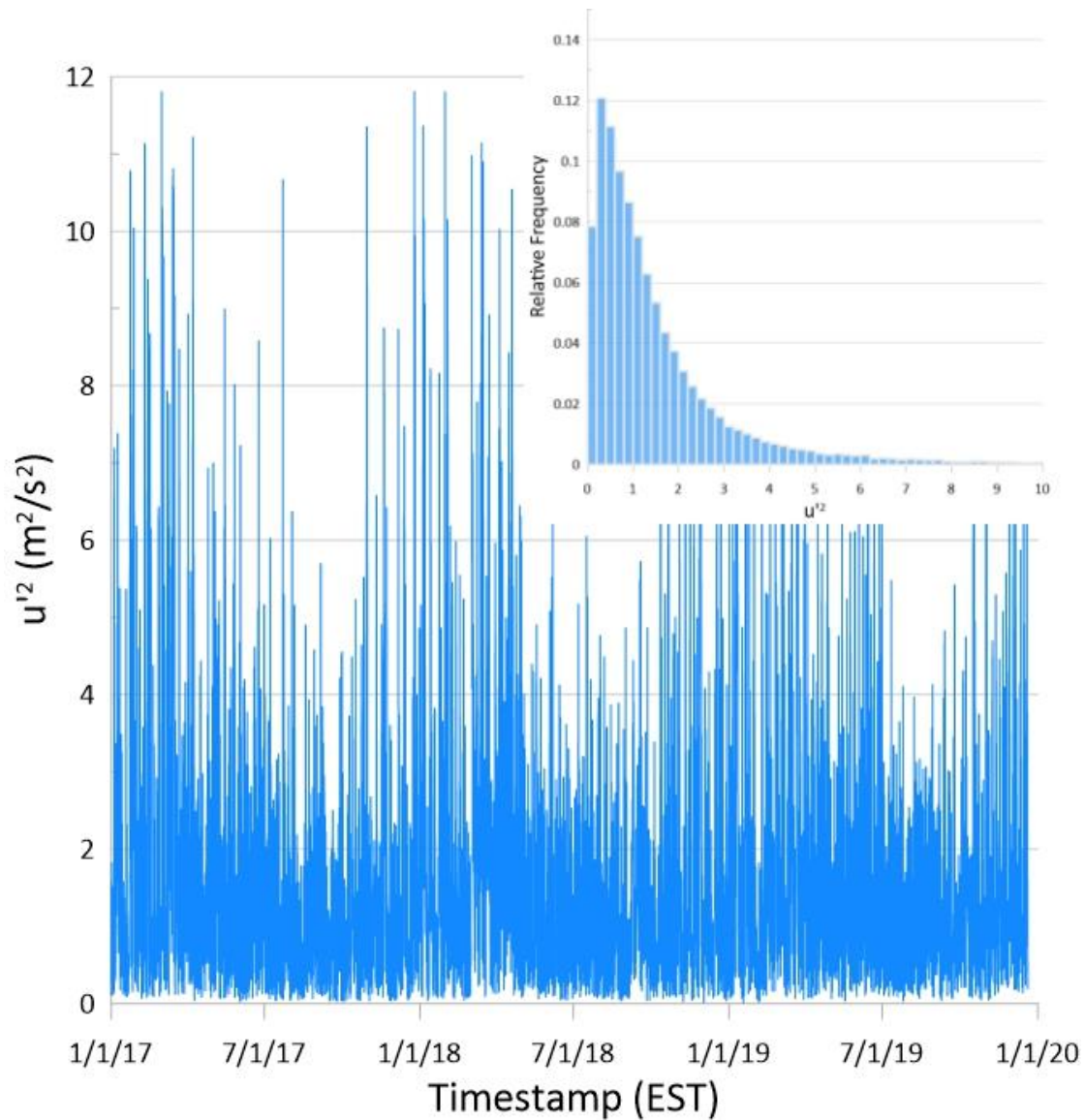
Figure 9: Measured 15-minute average horizontal u-component velocity variance for the period 1/1/2017 through 12/31/2019. For presentation clarity,every tenth data point displayed. The insert graph provides a histogram of accepted observed u-component velocity variance based on the outlier identification process.
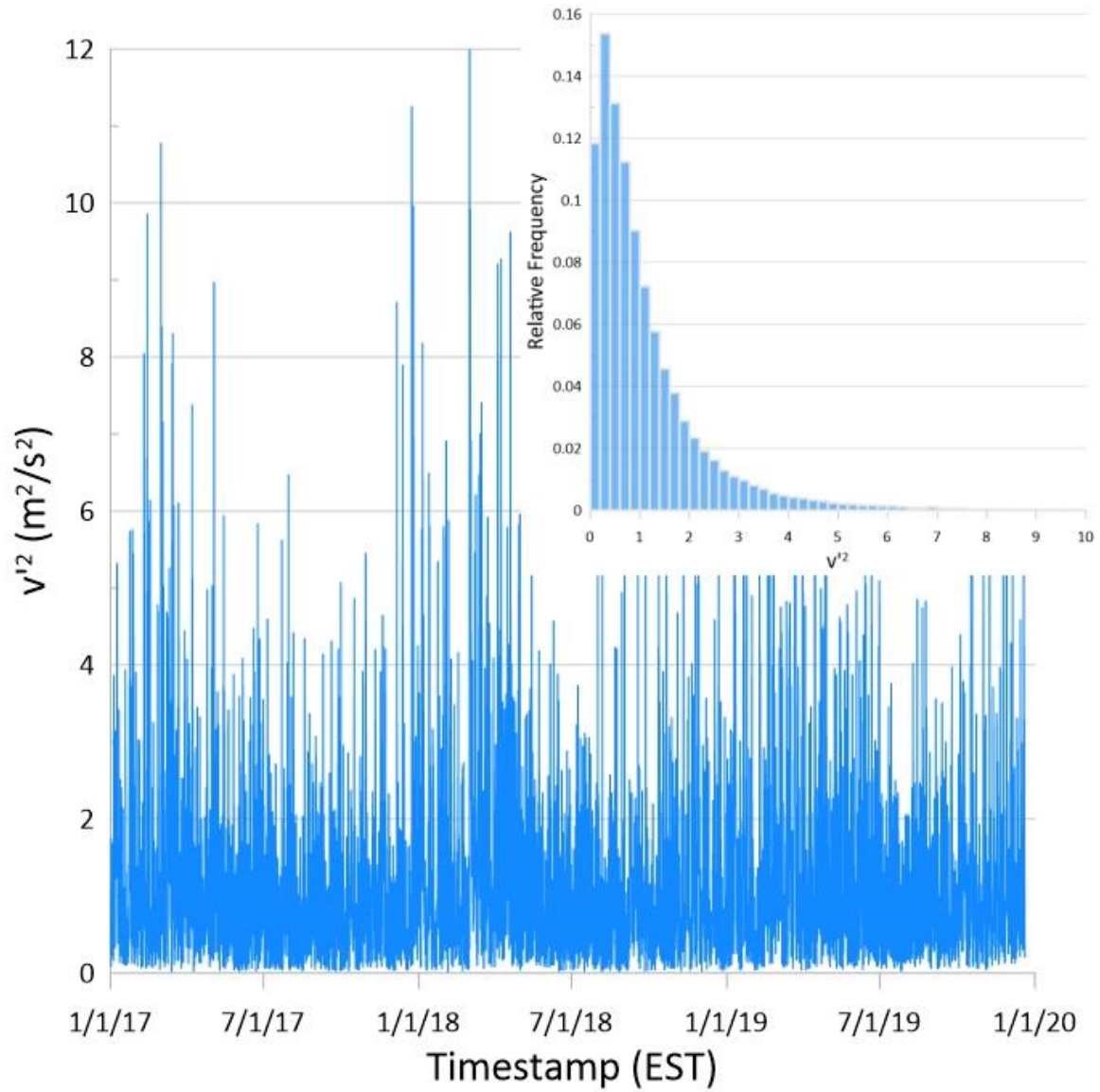
Figure 10: Measured 15-minute average horizontal v-component velocity variance for the period 1/1/2017 through 12/31/2019. For presentation clarity,every tenth data point displayed. The insert graph provides a histogram of accepted observed v-component velocity variance based on the outlier identification process.
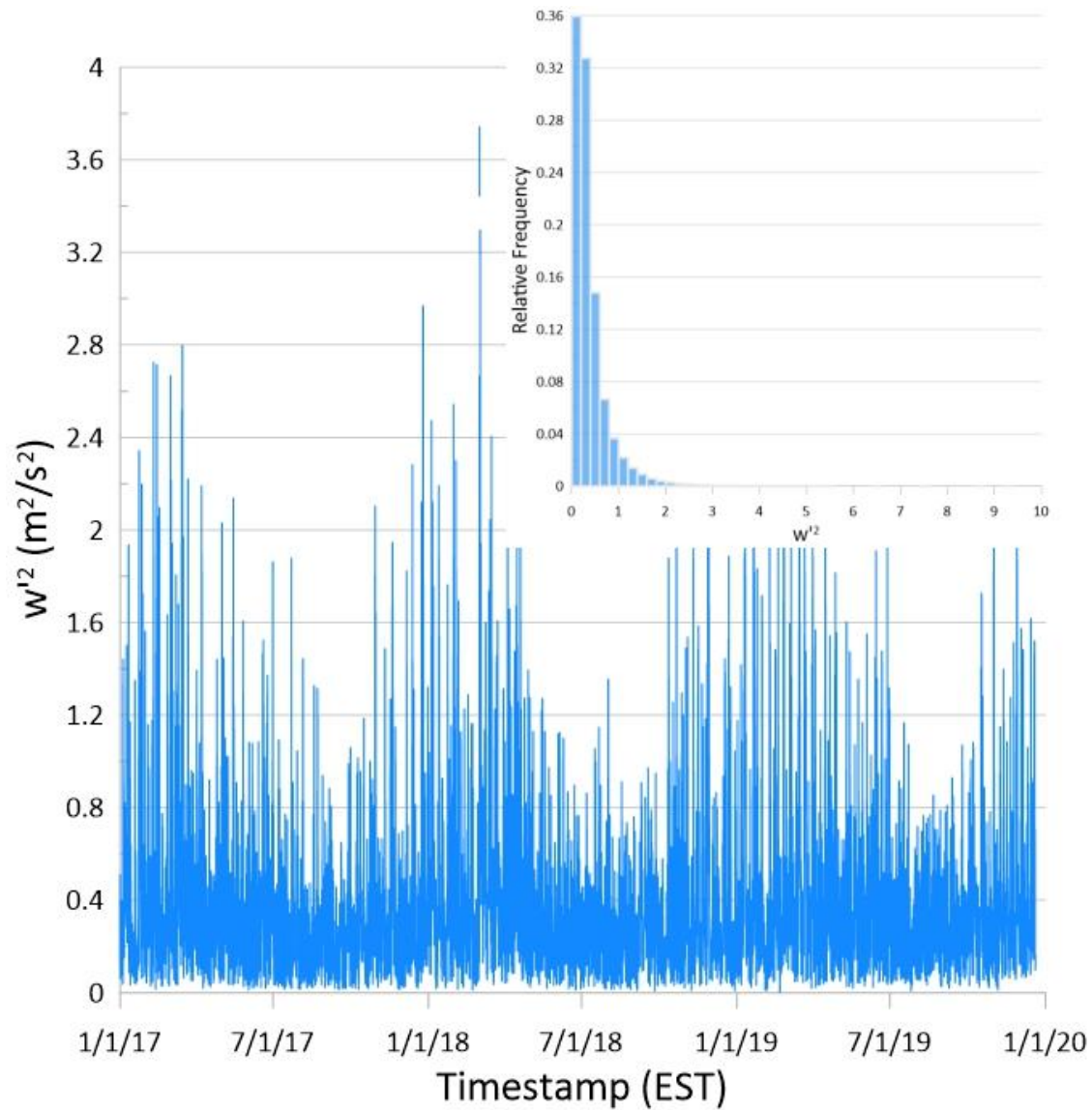
Figure 11: Measured 15-minute average vertical w-component velocity variance for the period 1/1/2017 through 12/31/2019. For presentation clarity, every tenth data point displayed. The insert graph provides a histogram of accepted observed w-component velocity variance based on the outlier identification process.
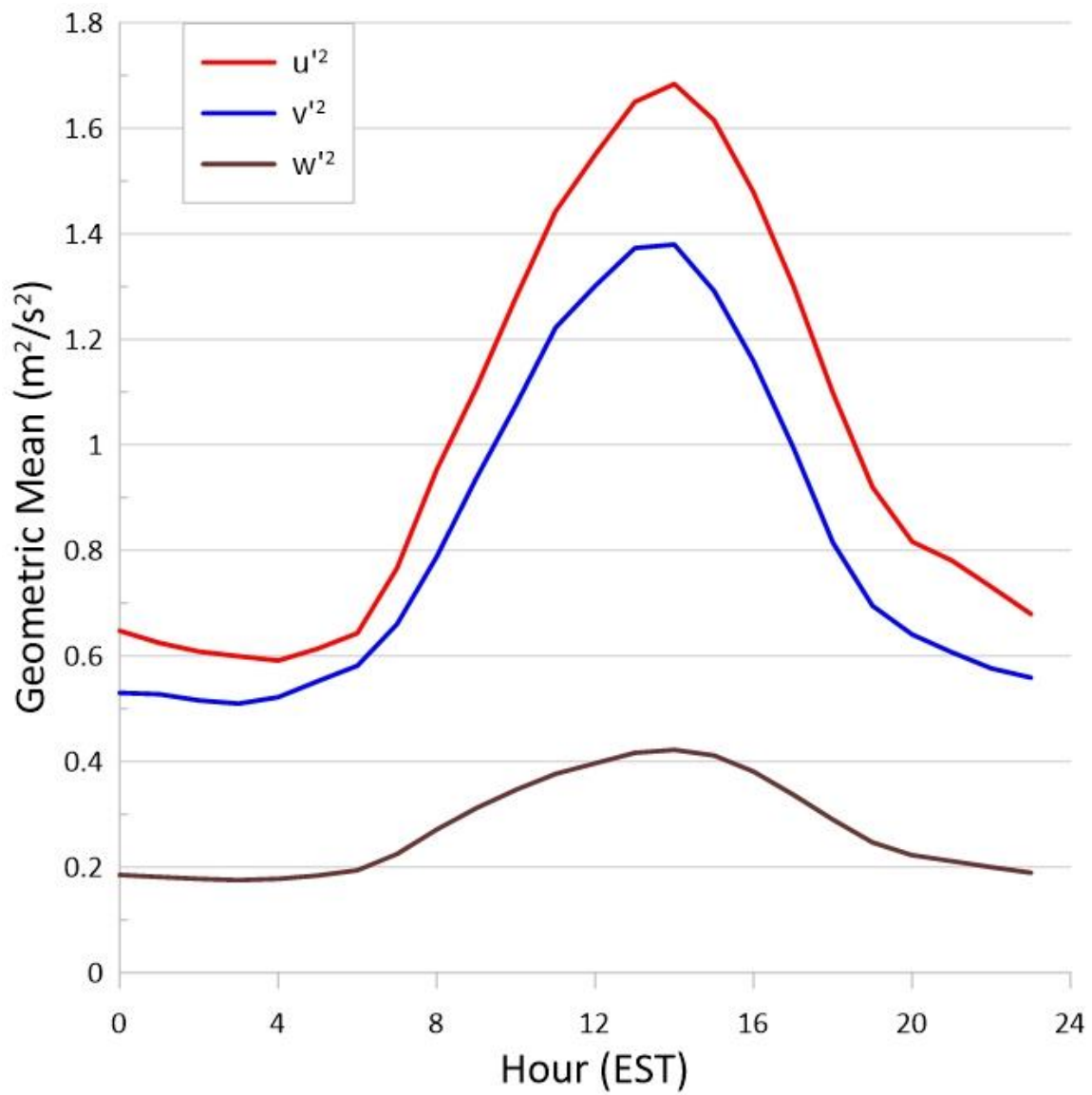
Figure 12: Geometric mean of both horizontal and vertical turbulence observations.
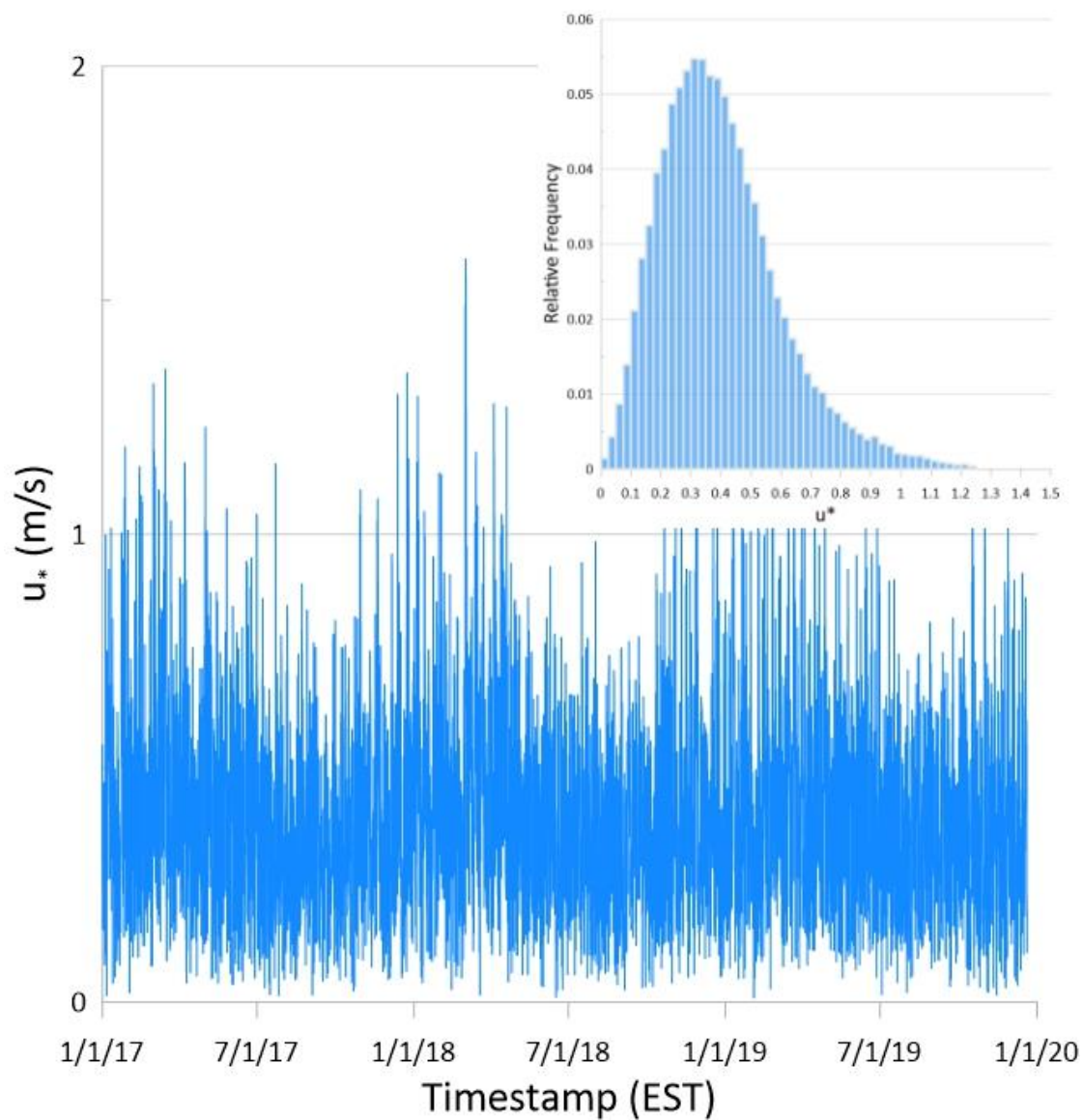
Figure 13: Measured 15-minute (shear-stress)$^{0.5}$ or u_* for the period 1/1/2017 through 12/31/2019. For presentation clarity,every tenth data point displayed. The insert graph provides a histogram of accepted observed u_* based on the outlier identification process.

Figure 14: Measured 15-minute heat flux (w'T') or Heat for the period 1/1/2017 through 12/31/2019. For presentation clarity,every tenth data point displayed. The insert graph provides a histogram of accepted observed Heat based on the outlier identification process.
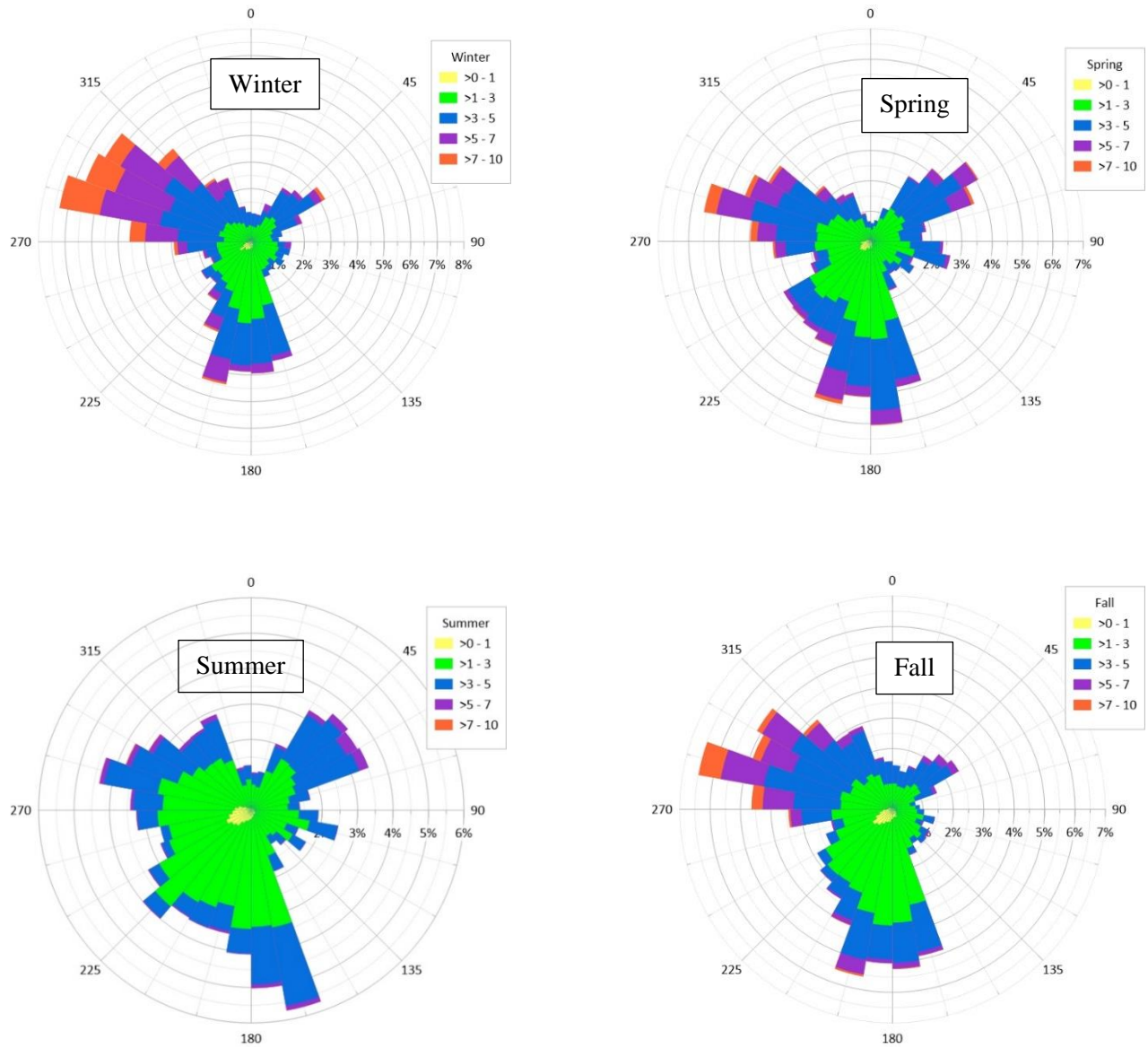
Figure 15: Hoover 2017 -2019 seasonal wind roses or wind speed/direction joint frequencies. Winter (January – March), Spring (April – June), Summer (July – September), Fall (October – December).
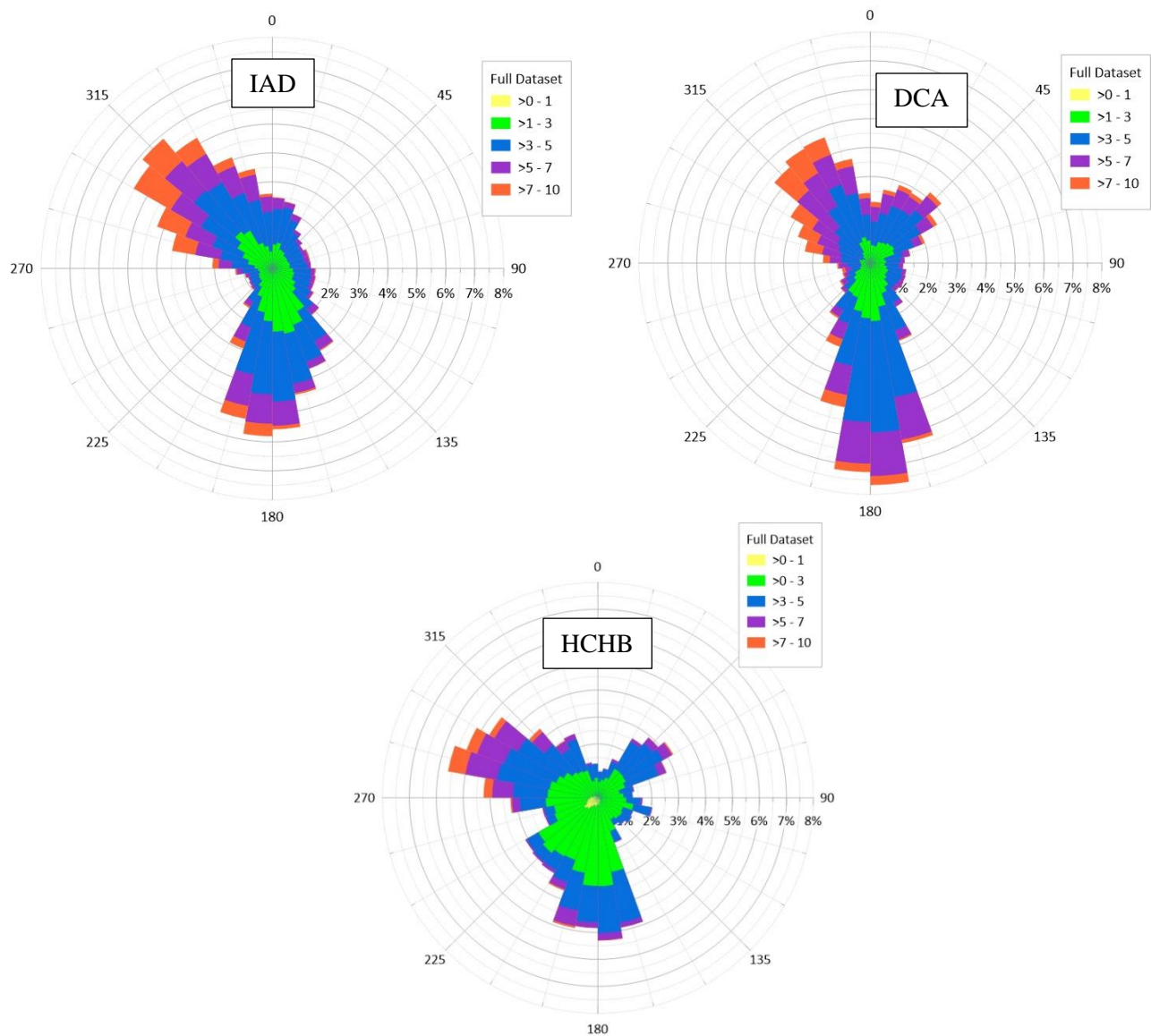
Figure 16: Comparison of 2017 – 2019 Joint wind speed/direction frequency plots for HCHB Hoover-North and the two nearest National Weather Service monitoring stations IAD (Dulles International Airport) and DCA (Reagan National Airport).
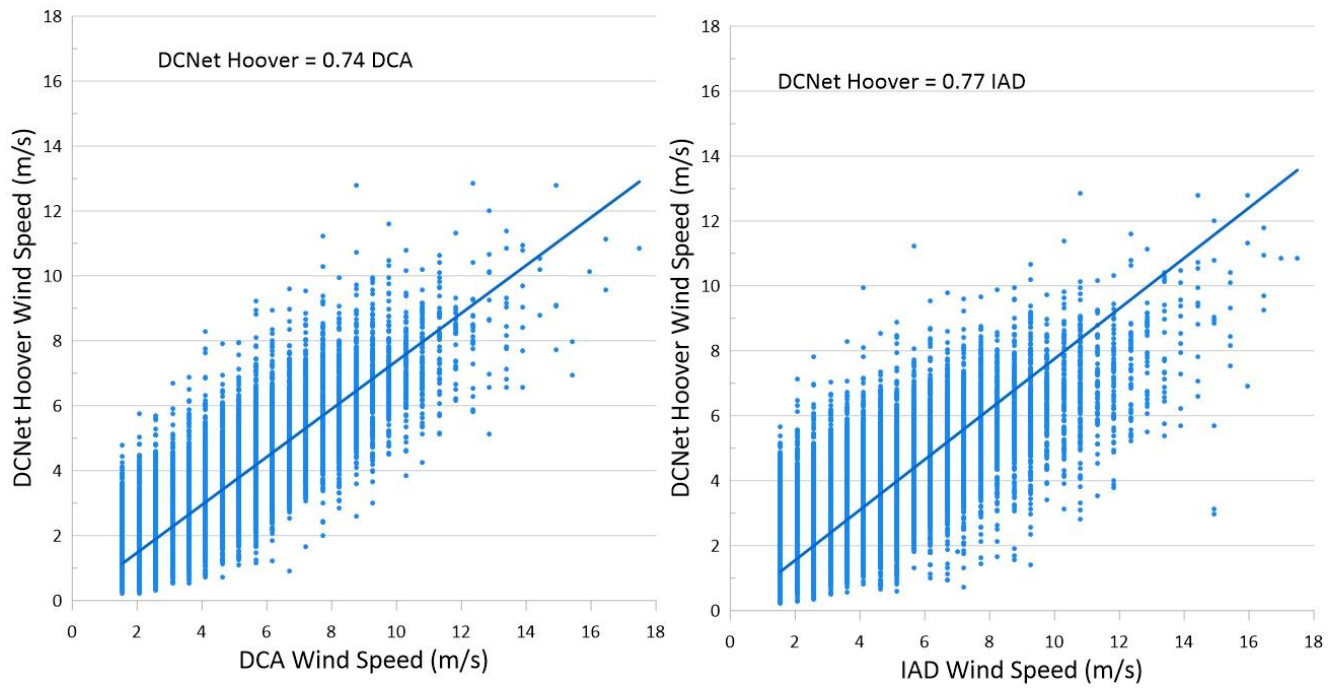
Figure 17: Linear regression of DCA and IAD measured wind speed against Hoover measured wind speed.
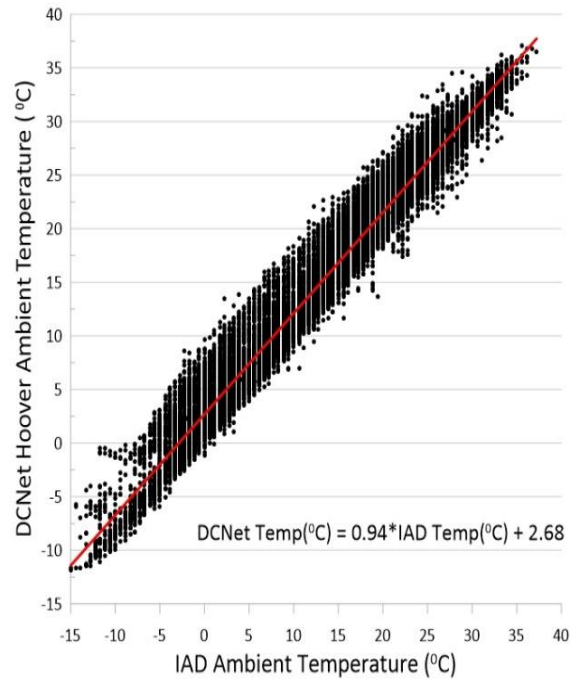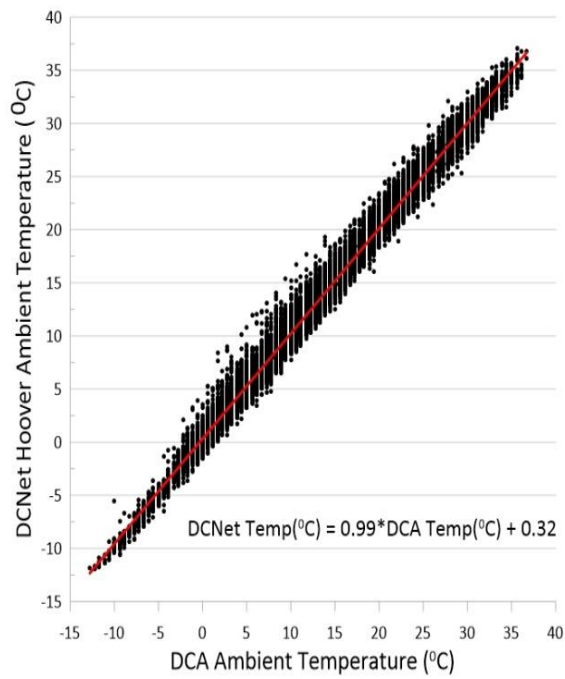
Figure 18: Simple linear regression of DCA and IAD measured temperature against Hoover observed temperatures.
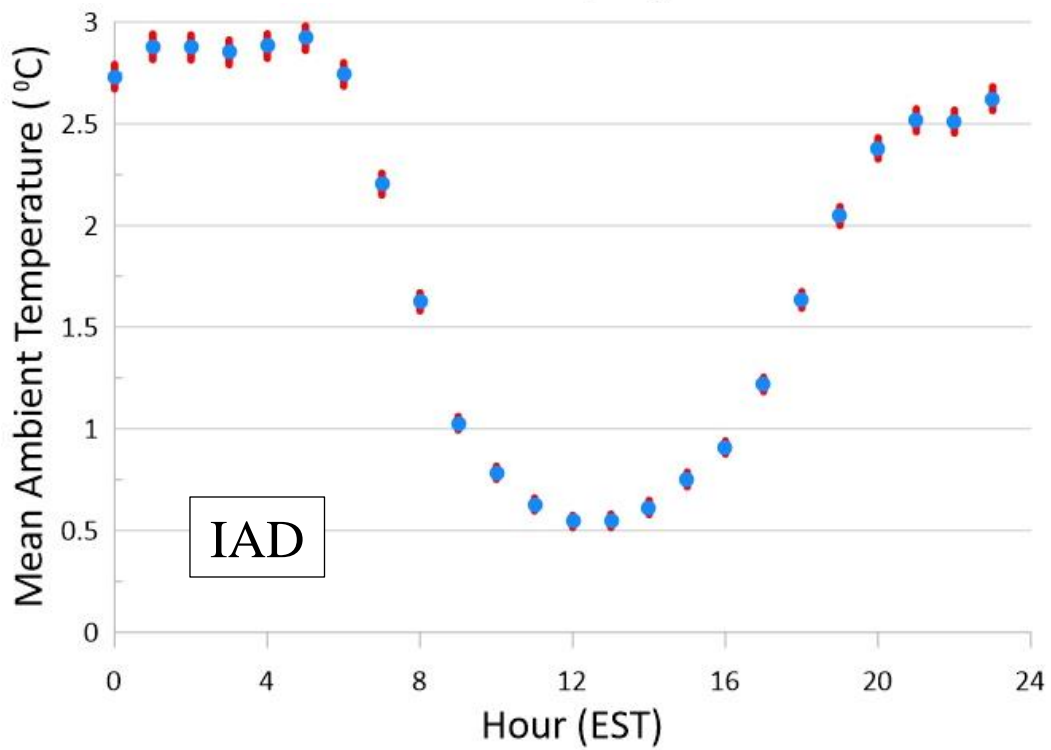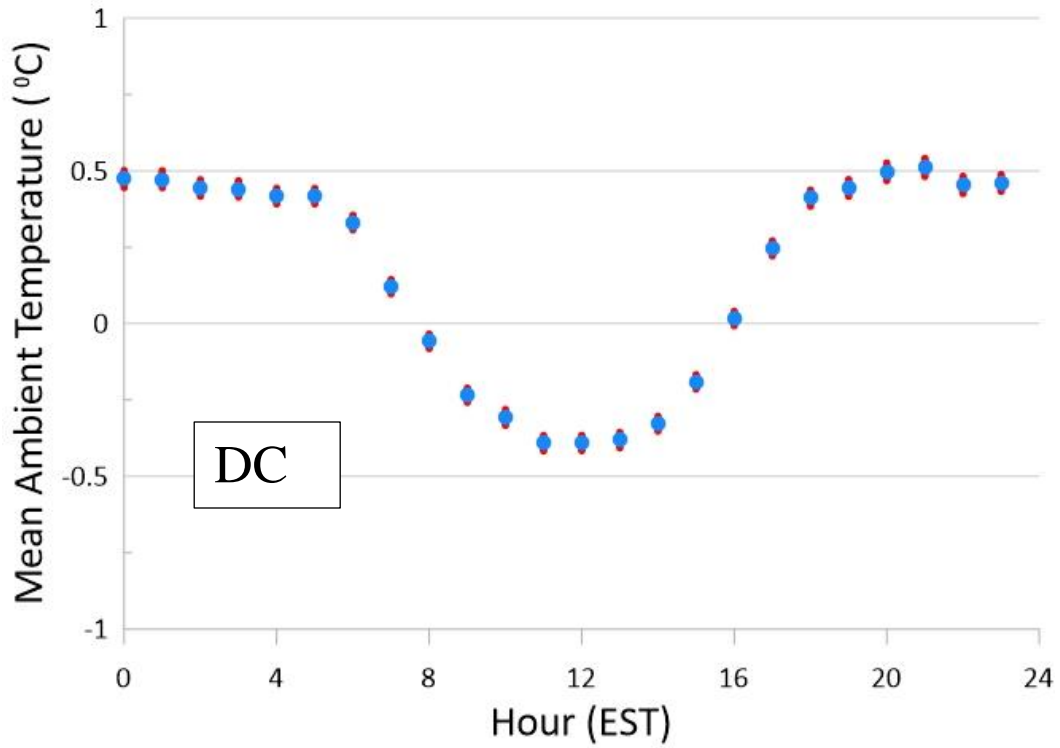
Figure 19: Mean ambient temperature difference by Hour between IAD, DCA and Hoover monitoring stations. (DCNet minus NWS)

(a) $u^* = 0.13\ U$

(b)
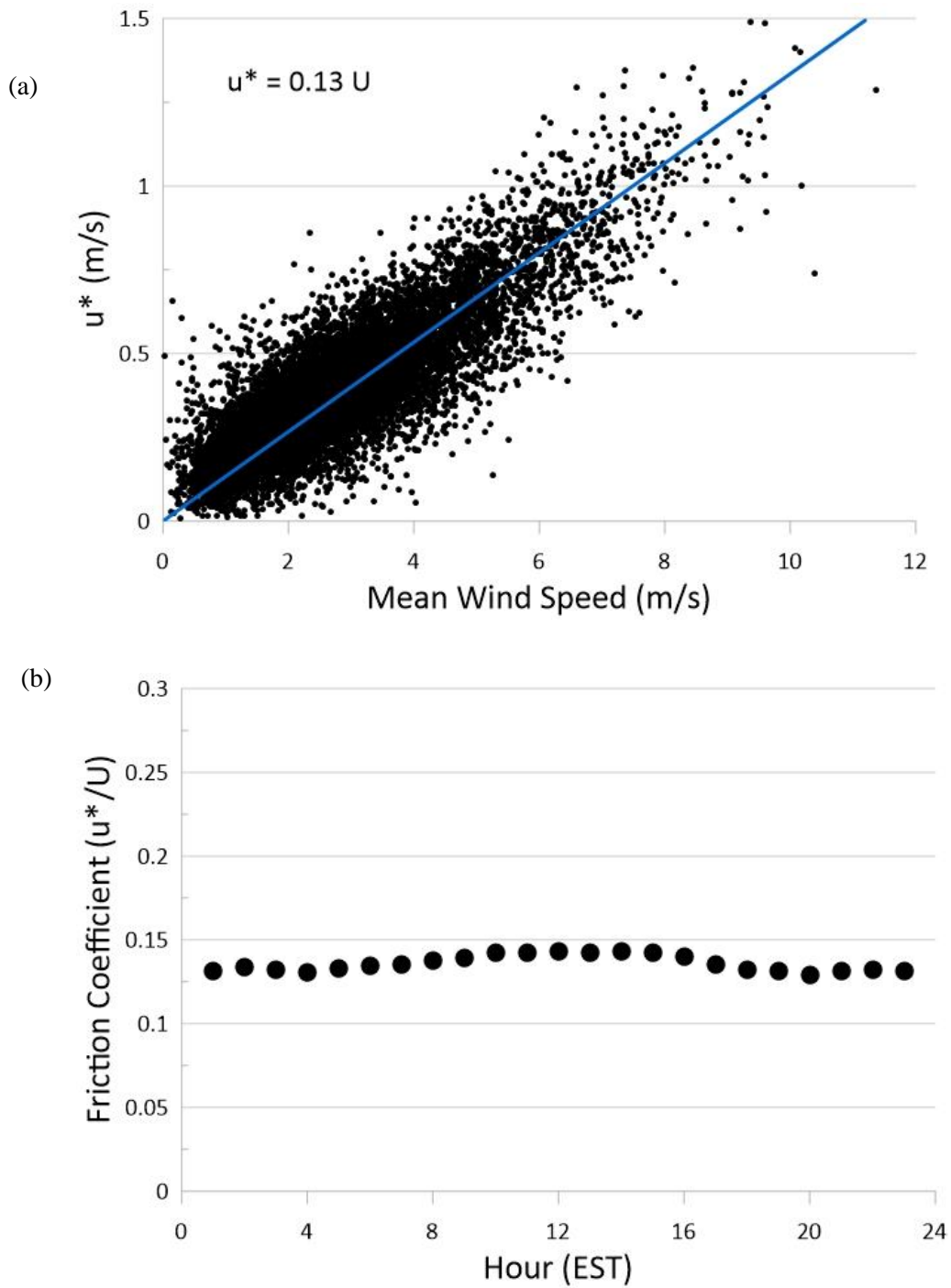
Figure 20: Hoover friction coefficient (a) regression analysis (b) geometric mean by hour (EST) of the day
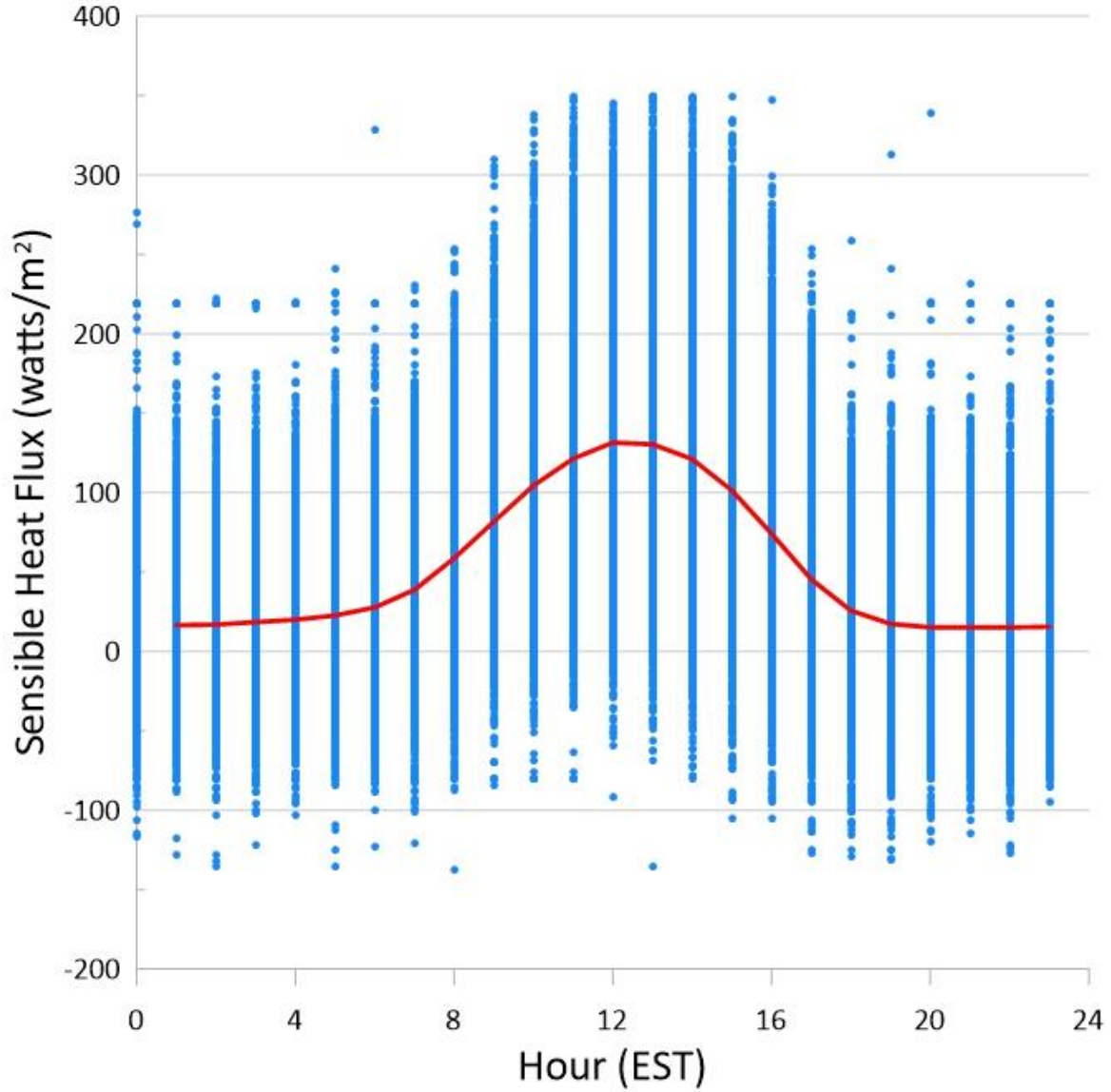
Figure 21: Hoover sensible heat flux by hour (EST) the red line is the mean heat flux binned by hours of the day.
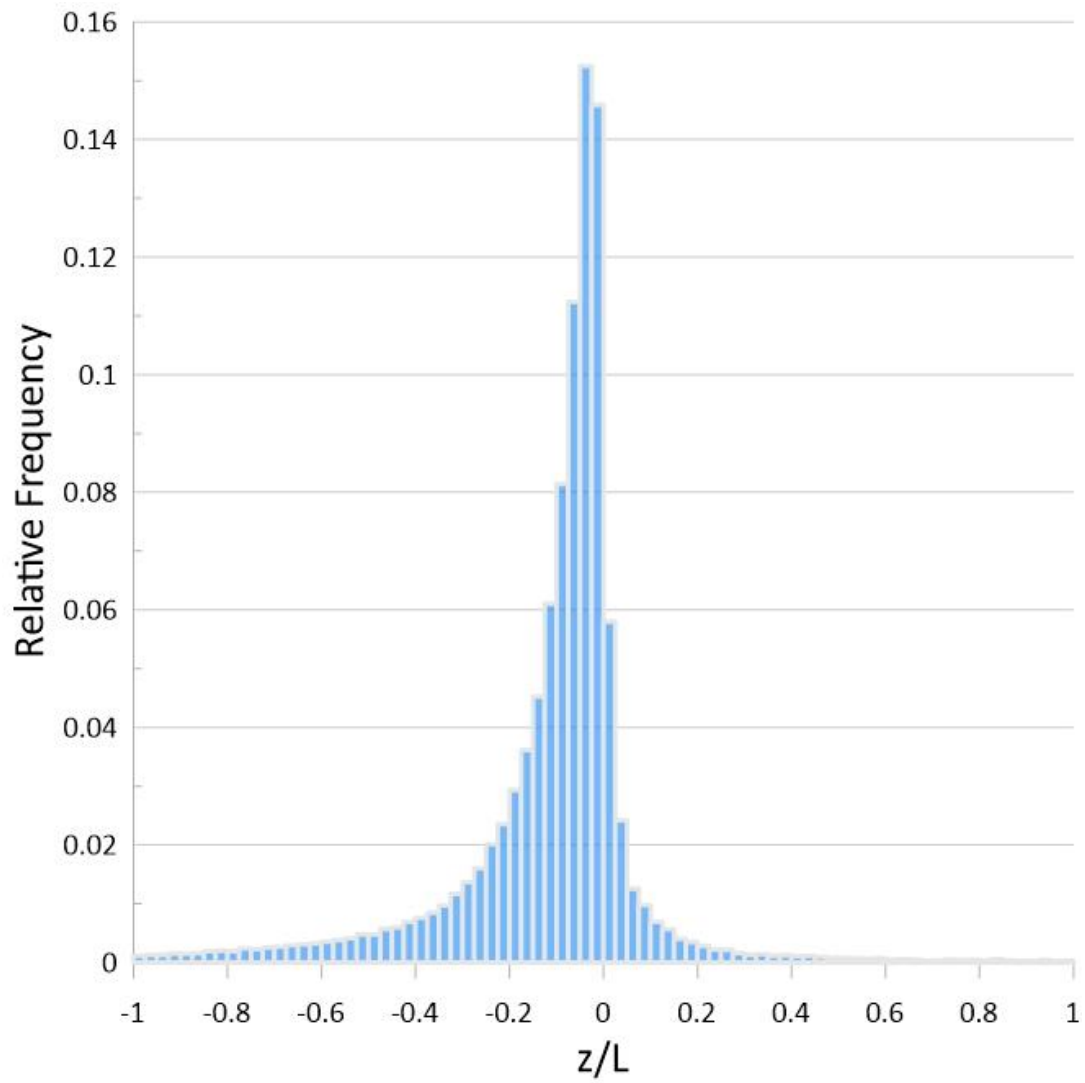
Figure 22: Histogram of Hoover Monin-Obukhov stability (z/L)
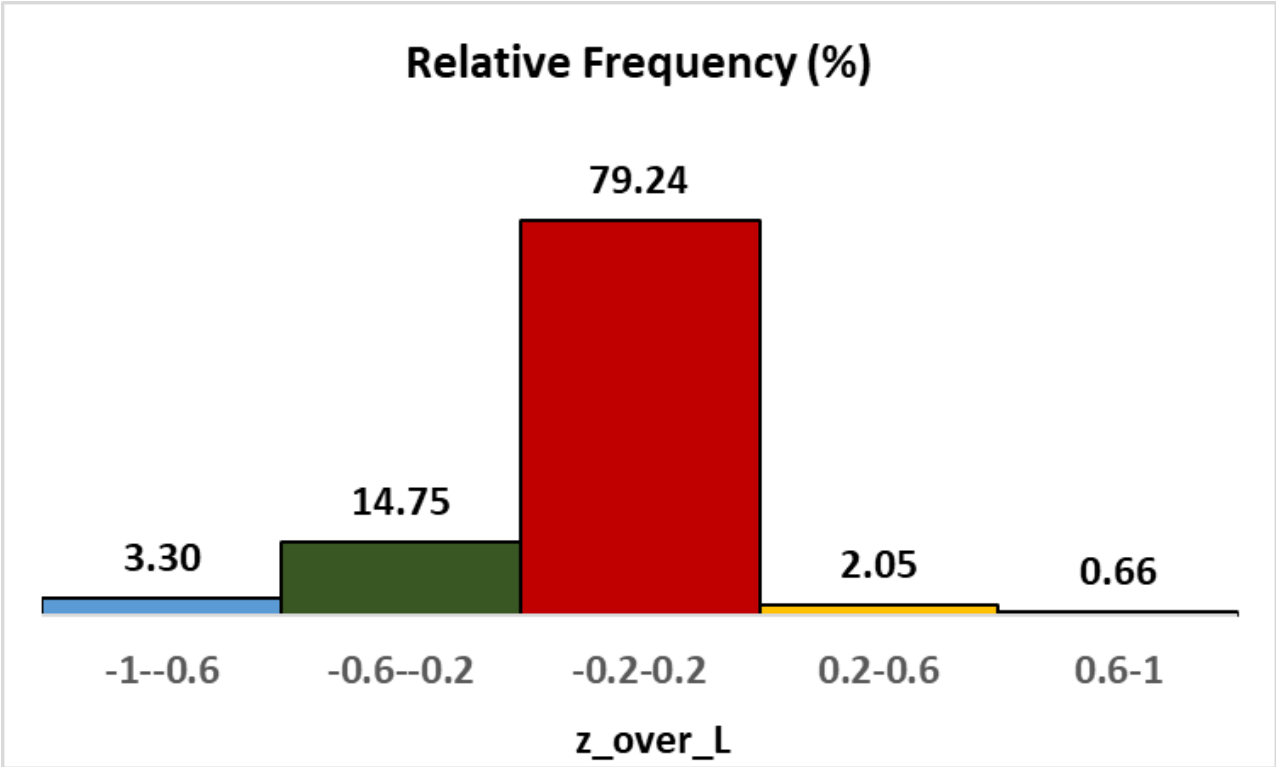
Figure 23: Partition of Monin-Obukhov stability for the Hoover station.
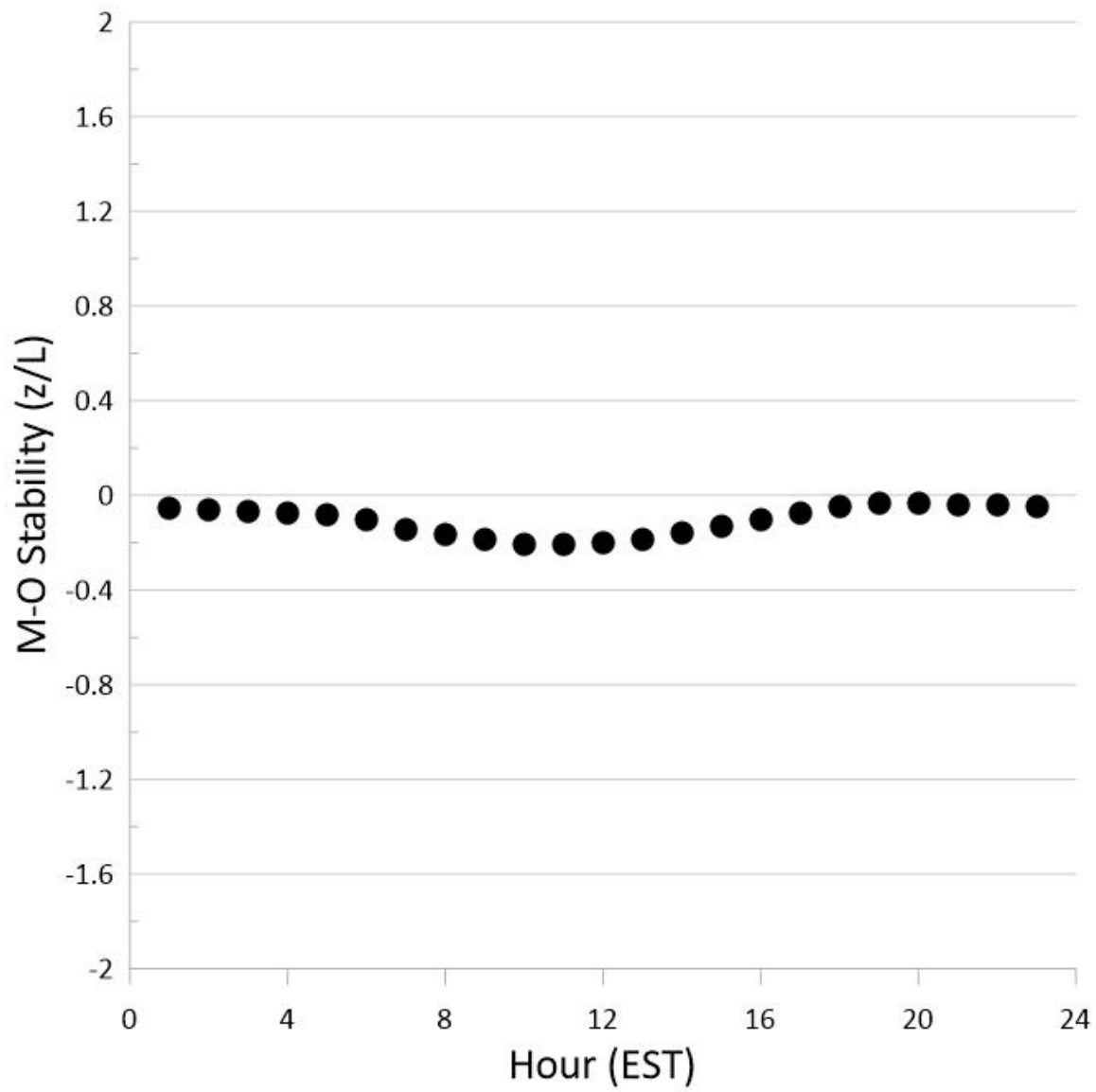
Figure 24 Mean Monin-Obukhov stability (z/L) as a function of time of day.
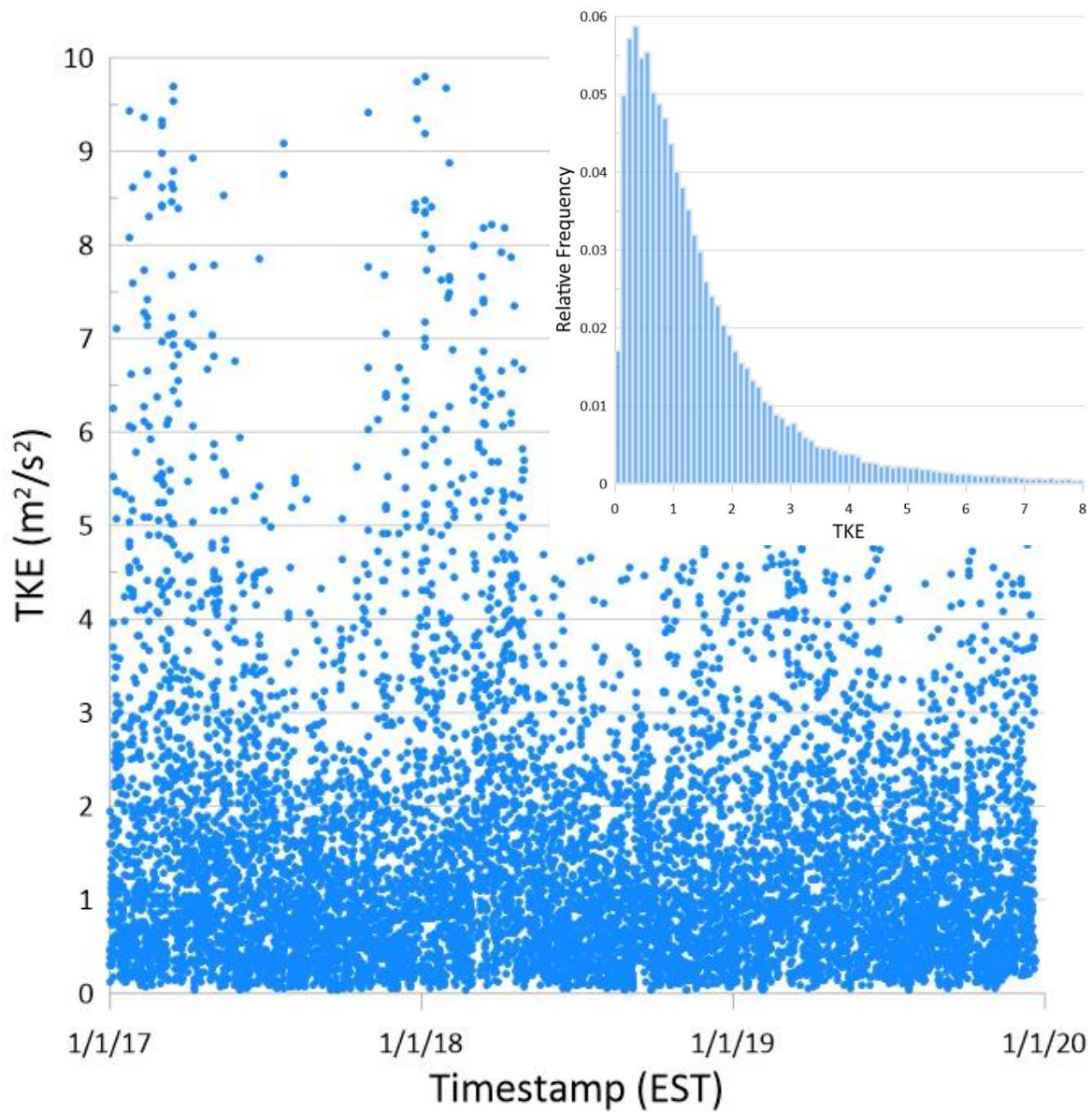
Figure 25: Calculated 15-minute average turbulent kinetic energy (TKE) for the period 1/1/2017 through 12/31/2019. For presentation clarity,every tenth data point displayed. The insert graph provides a histogram of accepted calculated TKE based on the outlier identification process.
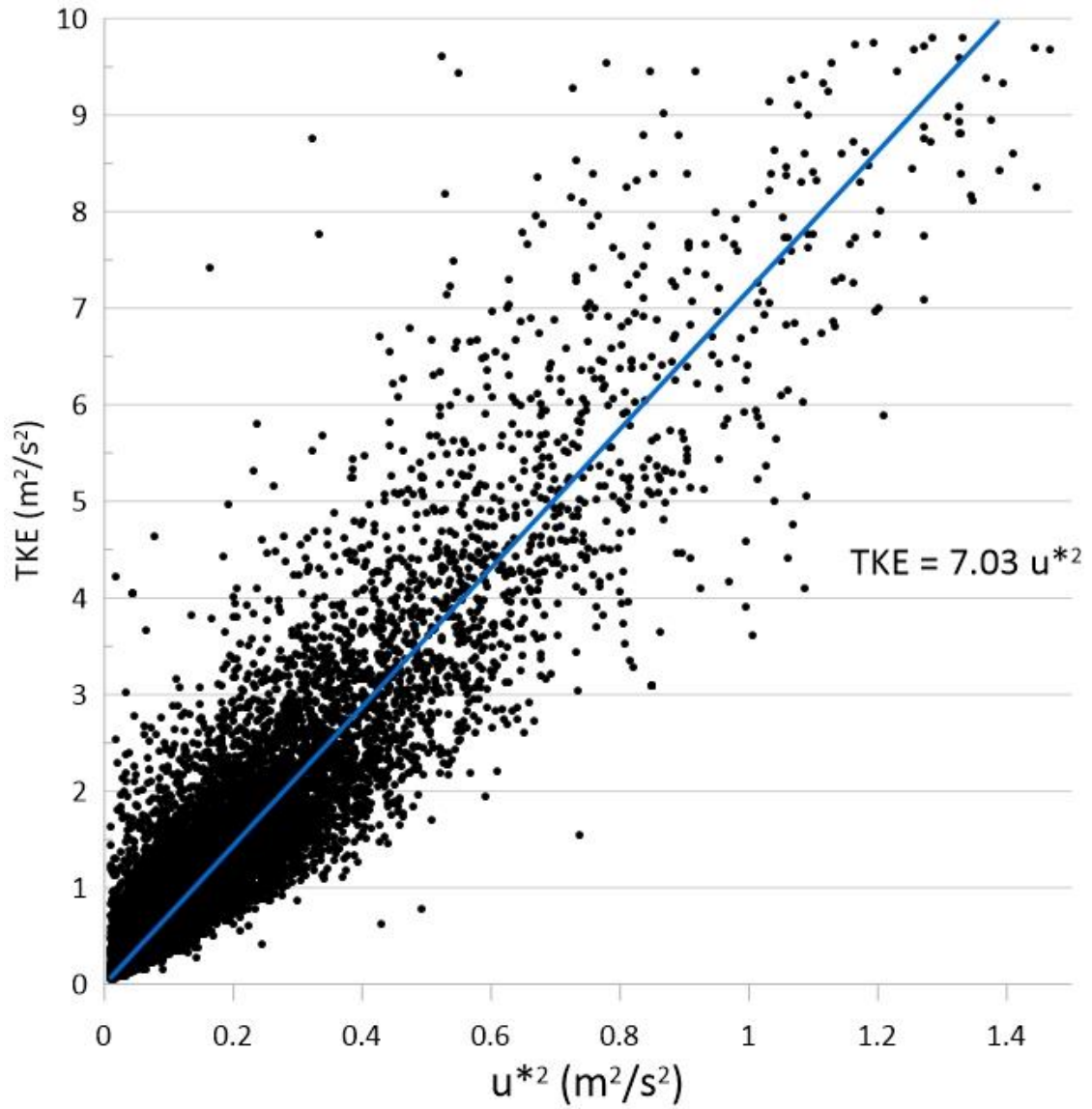
Figure 26: Regression analysis of TKE (turbulent kinetic energy) against u_*^2 (shear stress – u'w') for the period 1/1/2017 through 12/31/2019. For presentation clarity,every tenth data point displayed.
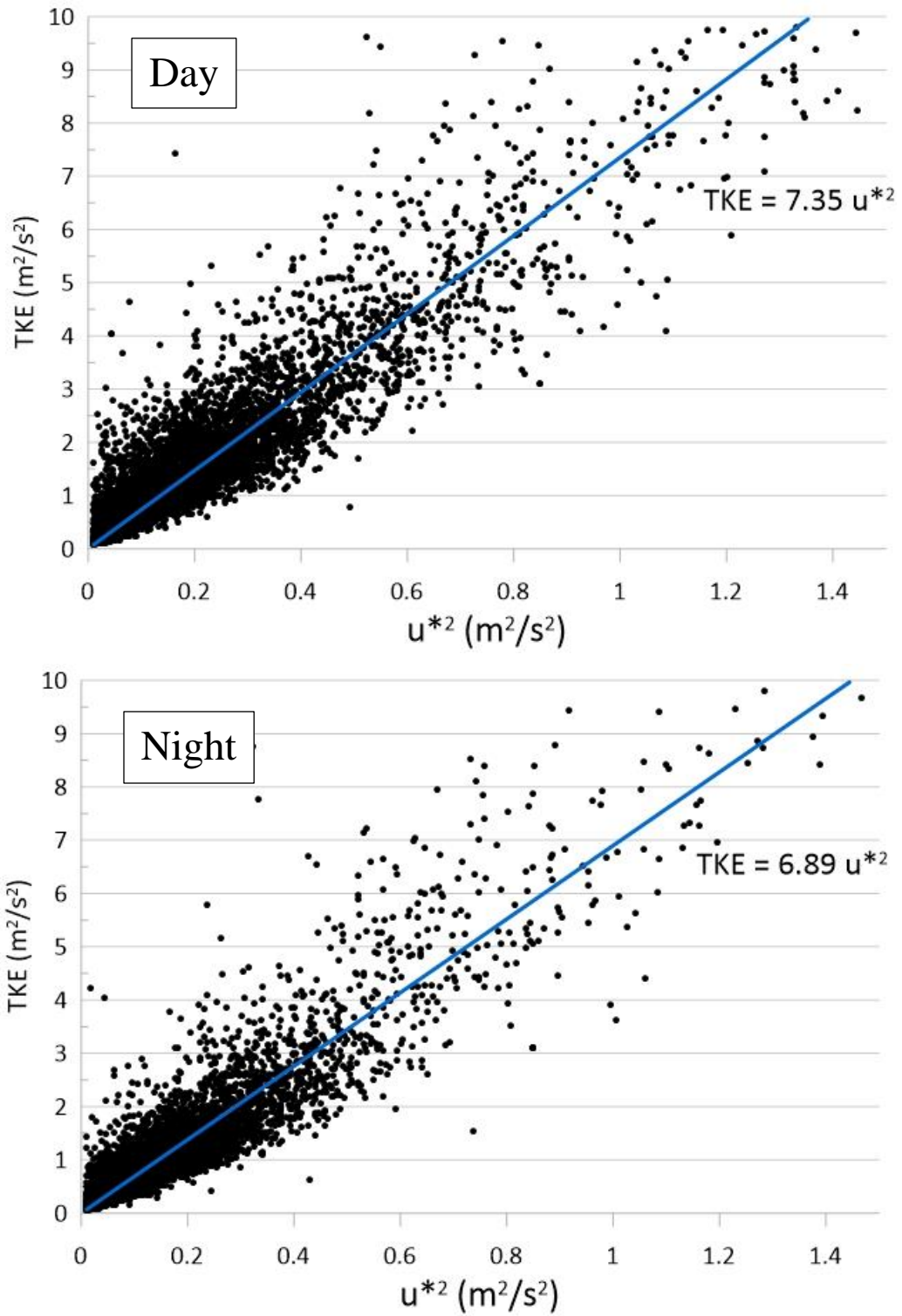
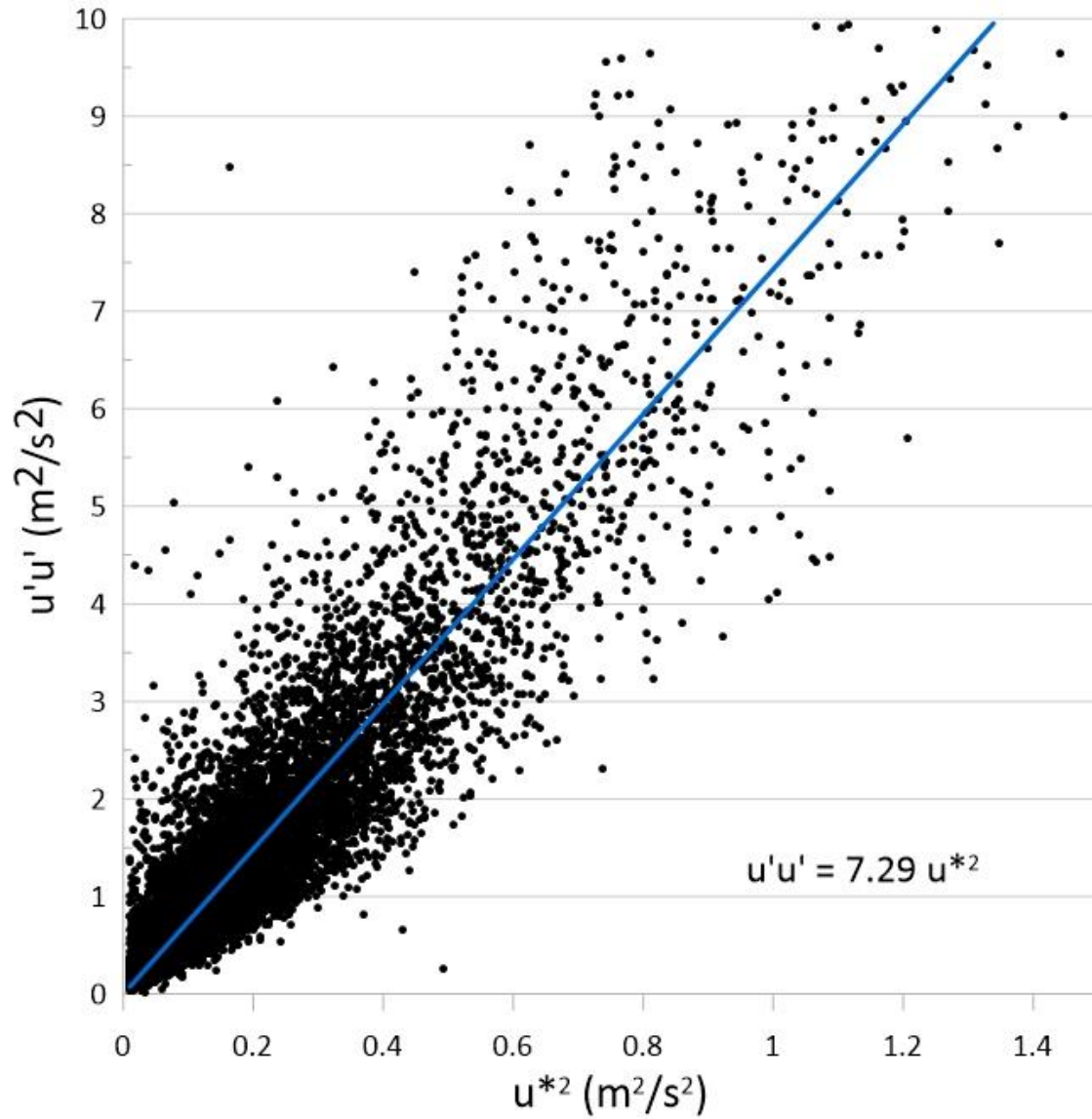Figure 27: Nighttime and daytime correlations of TKE against u_*^2 .

Figure 28: Regression analysis of u_*^2 (horizontal velocity variance velocity u-component) against u_*^2 (shear stress – u'w') for the period 1/1/2017 through 12/31/2019. For presentation clarity, every tenth data point displayed.
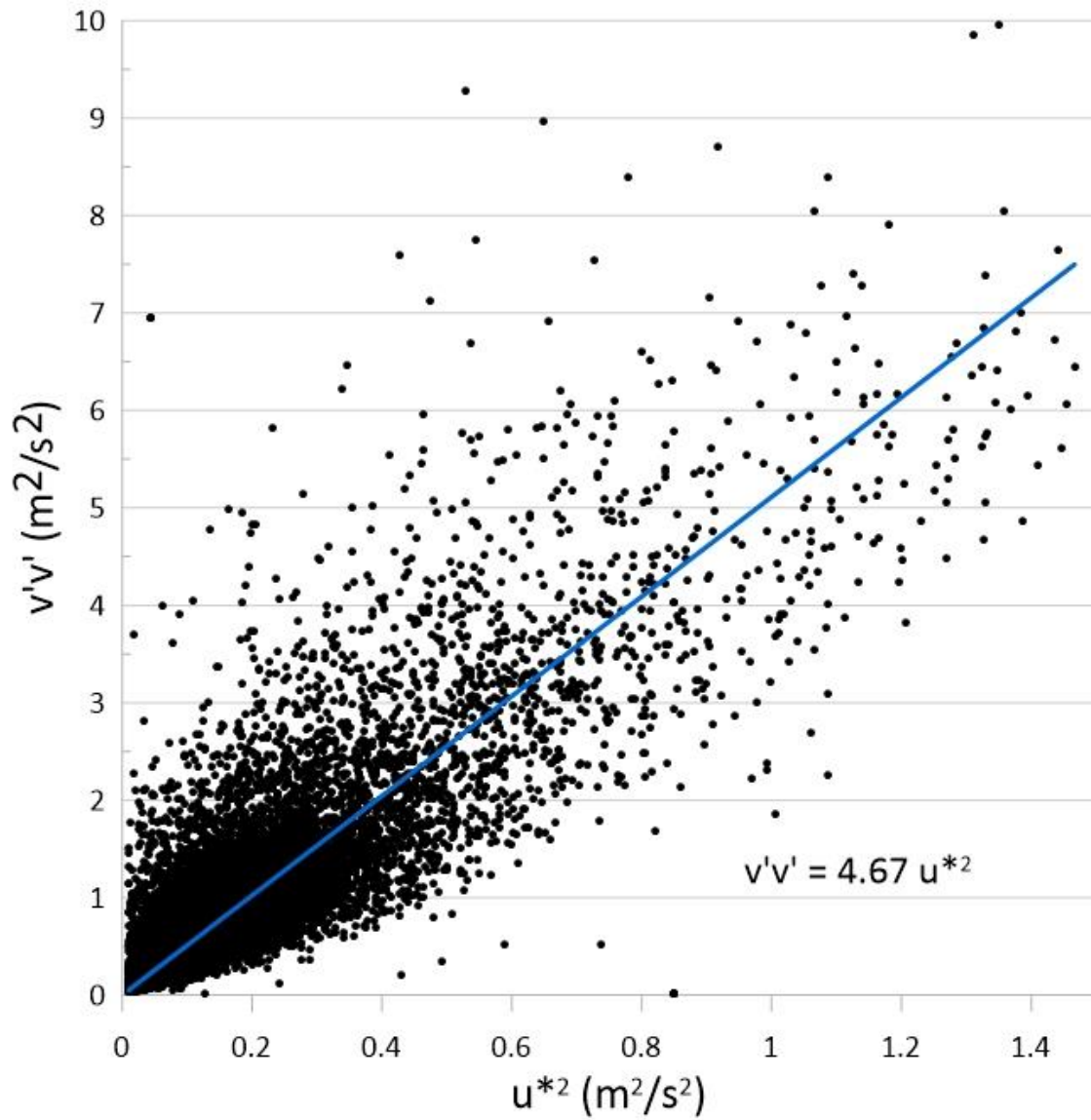
Figure 29: Regression analysis of v'^{2} (horizontal velocity variance velocity v-component) against u_*^2 (shear stress – u'w') for the period 1/1/2017 through 12/31/2019. For presentation clarity,every tenth data point displayed.
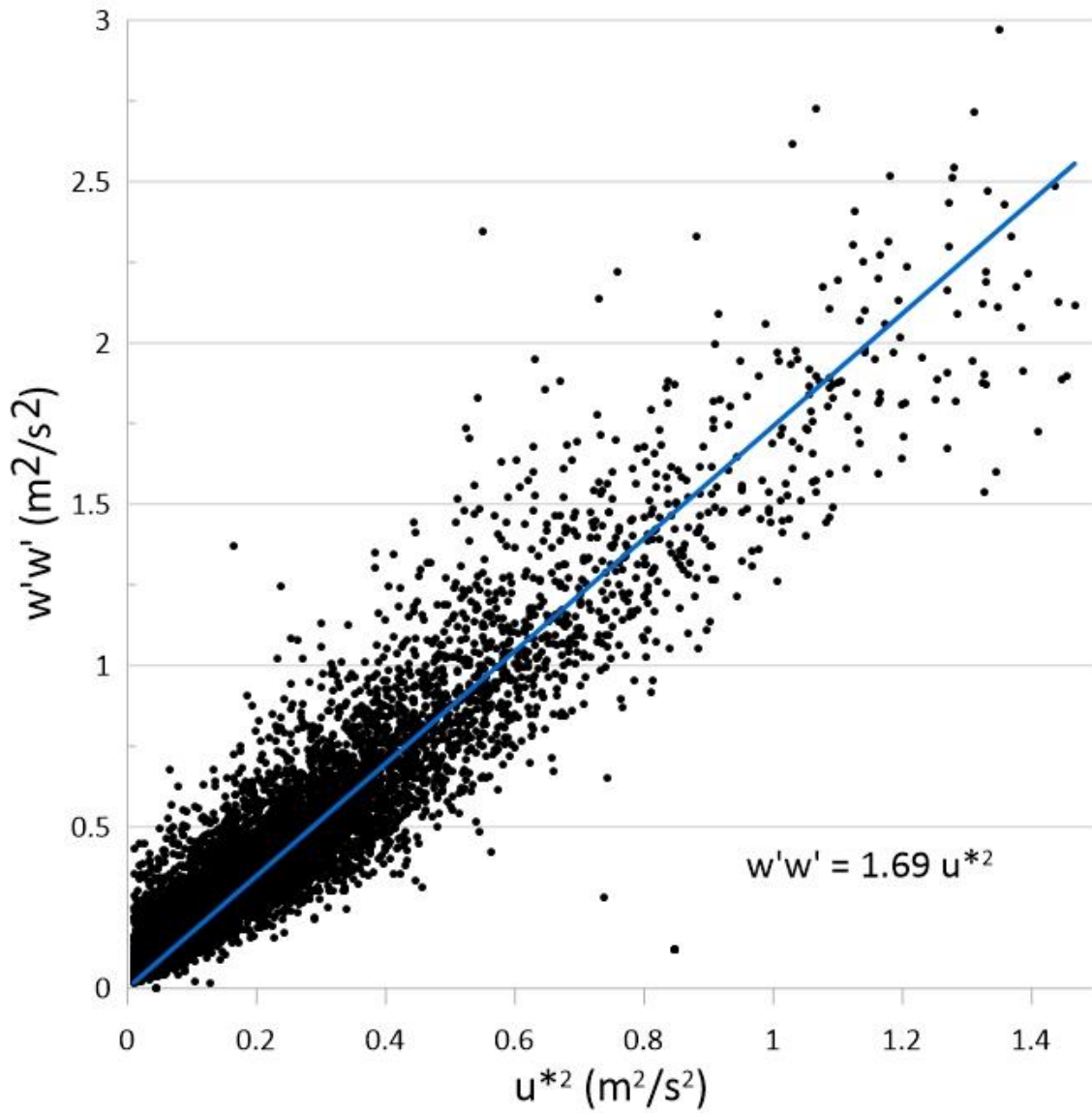
Figure 30: Regression analysis of w'^{2} (vertical velocity variance velocity component) against u_*^2 (shear stress – u'w') for the period 1/1/2017 through 12/31/2019. For presentation clarity, every tenth data point displayed.